# Toward a complete Himalayan hydrological budget: Spatiotemporal distribution of snowmelt and rainfall and their impact on river discharge

Bodo Bookhagen[1] and Douglas W. Burbank[2]

Received 26 June 2009; revised 9 February 2010; accepted 23 March 2010; published 10 August 2010.

[1] The hydrological budget of Himalayan rivers is dominated by monsoonal rainfall and snowmelt, but their relative impact is not well established because this remote region lacks a dense gauge network. Here, we use a combination of validated remotely-sensed climate parameters to characterize the spatiotemporal distribution of rainfall, snowfall, and evapotranspiration in order to quantify their relative contribution to mean river discharge. Rainfall amounts are calculated from calibrated, orbital, high-resolution Tropical Rainfall Measurement Mission data, and snow-water equivalents are computed from a snowmelt model based on satellite-derived snow cover, surface temperature, and solar radiation. Our data allow us to identify three key aspects of the spatiotemporal precipitation pattern. First, we observe a strong decoupling between the rainfall on the Himalayan foreland versus that in the mountains: a pronounced sixfold, east-west rainfall gradient in the Ganges plains exists only at elevations <500 m asl. Mountainous regions (500 to 5000 m asl) receive nearly equal rainfall amounts along strike. Second, whereas the Indian summer monsoon is responsible for more than 80% of annual rainfall in the central Himalaya and Tibetan Plateau, the eastern and western syntaxes receive only ~50% of their annual rainfall during the summer season. Third, snowmelt contributions to discharge differ widely along the range. As a fraction of the total annual discharge, snowmelt constitutes up to 50% in the far western (Indus area) catchments, ~25% in far eastern (Tsangpo) catchments, and <20% elsewhere. Despite these along-strike variations, snowmelt in the pre- and early-monsoon season (April to June) is significant and important in all catchments, although most pronounced in the western catchments. Thus, changes in the timing or amount of snowmelt due to increasing temperatures or decreasing winter precipitation may have far-reaching societal consequences. These new data on precipitation and runoff set the stage for far more detailed investigations than have previously been possible of climate-erosion interactions in the Himalaya.

**Citation:** Bookhagen, B., and D. W. Burbank (2010), Toward a complete Himalayan hydrological budget: Spatiotemporal distribution of snowmelt and rainfall and their impact on river discharge, *J. Geophys. Res.*, *115*, F03019, doi:10.1029/2009JF001426.

## 1. Introduction

[2] The Himalaya and adjacent Tibetan Plateau are the source of several major Asian rivers supporting a large, diverse ecosystem and a population of more than 1 billion people [*Ives and Messerli*, 1989]. Large rivers such as the Indus, Sutlej, Ganges, Arun, and Brahmaputra/Tsangpo draining the southern Tibetan Plateau and the Himalaya (Figure 1) are essential for agriculture and energy generation and are the pathways for sediments leaving the orogen. The precipitation in the upstream and high-elevation parts of these basins falls as snow, causing a natural delay in the river discharge. Snow-cover dynamics in the High Himalaya and on the Tibetan Plateau, therefore, influence the water availability downstream in the major river basins of Asia, specifically in the spring at the onset of the growing season, but also in the fall after the monsoon season [*Barnett et al.*, 2005; *Güntner et al.*, 2007; *Immerzeel et al.*, 2009; *Kundzewicz et al.*, 2007; *Lemke et al.*, 2007; *Viviroli et al.*, 2007; *Singh and Kumar*, 1997]. In the Himalayan foreland and at low to moderate elevations, precipitation is dominated by rainfall during the Indian summer monsoon season [*Anders et al.*, 2006; *Bookhagen et al.*, 2005a; *Bookhagen and Burbank*, 2006]. Along the southern Himalayan front, a strong south-to-north rainfall gradient exists with wet,

[1]Geography Department, University of California, Santa Barbara, California, USA.
[2]Institute for Crustal Studies, University of California, Santa Barbara, California, USA.

Copyright 2010 by the American Geophysical Union.
0148-0227/10/2009JF001426

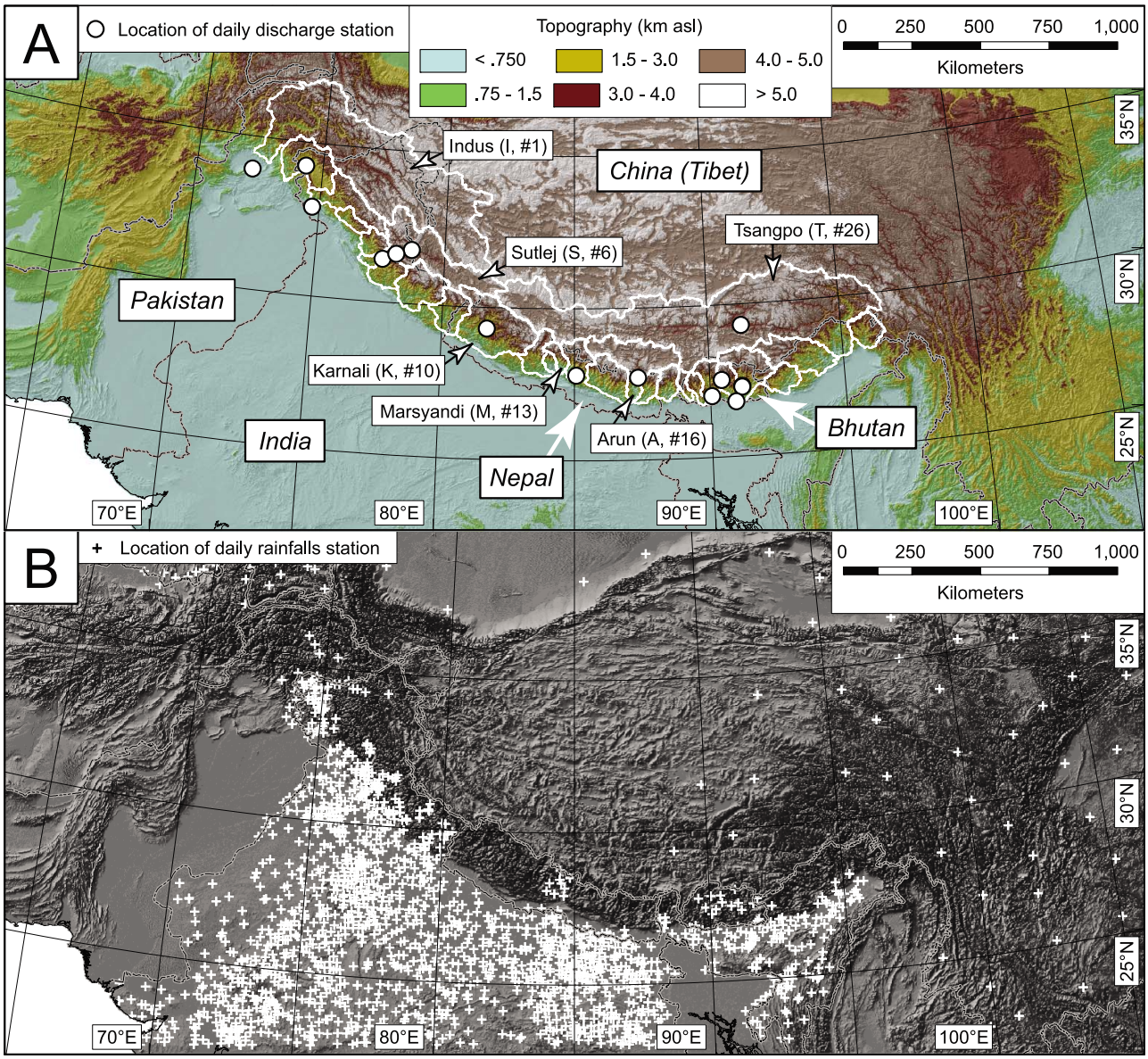


**Figure 1.** (a) Topographic map showing the study area and the 27 major catchments draining the Himalaya to the south. White circles indicate river-discharge stations with daily measurements and labels mark reference catchments and river names. (b) Shaded-relief topography and daily rain-gauge locations used for TRMM rainfall calibration (n = 1741). Note the high-elevation stations in western India, central Nepal, and Bhutan.

southern areas near the Ganges Plains and arid, northern regions toward the Tibetan Plateau [*Burbank et al.*, 2003].

[3] In this paper we explore the relative spatiotemporal influence of snowmelt, rainfall, and evapotranspiration on river flow. We focus our analyses on 27 major catchments draining the southern Himalayan front, stretching from the Indus in the west to the Tsangpo/Brahmaputra River in the east (Figure 1a). We use high-resolution, calibrated, remotely sensed rainfall values combined with a simple, but robust snowmelt model based on satellite-derived snow cover, land-surface temperature, and solar radiation to quantify relative discharge contributions. We validate our results with daily river-gauge stations spanning the entire Himalayan front.

[4] Overall, our analysis reveals five important attributes of Himalayan precipitation and runoff. First, we have improved previous remotely sensed TRMM (Tropical Rainfall Measurement Mission) rainfall estimates [*Bookhagen and Burbank*, 2006] by using a dense network of more than 1700 ground-control stations as calibration locations, by accounting more completely for satellite orbital geometry, by developing an improved interpolation algorithm for the orbital data, and by including spatial error estimates for the data. Second, we demonstrate the importance of high-spatial resolution rainfall data to develop more robust rainfall-topography relations, and we demonstrate the significance of seasonal rainfall variations along strike of the Himalaya and their

implications for the hydrological budget. Third, we have processed remotely sensed lightning data from the TRMM-LIS (Lightning Image Sensor) satellite to identify regions of heavy convective activity that results in violent cloudbursts. We use these data in combination with rainfall-intensity measurements to outline regions where high-magnitude rainfall events are more common during the past decade. Fourth, in order to describe the hydrological budget of the Himalaya, we create a satellite-based snowmelt model that uses MODIS (Moderate Resolution Imaging Spectroradiometer) snow-cover data, land-surface temperatures, and solar radiation. We limit our analysis to the mountainous regions where evapotranspiration generally has a low impact on overall catchment hydrology (<10%). Nonetheless, we directly estimate evapotranspiration amounts from a MODIS product. Finally, river-gauge data indicate that, using our combined rainfall, snowmelt, and evapotranspiration model, we can predict average monthly discharge within <10% of their measured amounts. These predictions gain importance not only for understanding the hydrological budget, snowmelt magnitude, and timing of discharge, but also for studies using discharge as a predictor for fluvial erosion or as a key input for landscape evolution models.

## 2. Methods and Data Sets

### 2.1. Topographic Data

[5] We used the Shuttle Radar Topographic Mission (SRTM) Version 2 topographic data with a 90-m grid-cell size for our analysis [*Farr et al.*, 2007]. After filling holes in the SRTM data (See the auxiliary material for a more complete description of data processing), the entire, combined 90-m data set was hydrologically corrected using the method described by *Garbrecht and Martz* [1997].[1]

### 2.2. TRMM Rainfall

[6] We used raw, orbital satellite data from the Tropical Rainfall Measurement Mission (TRMM) to estimate rainfall amounts [*Kummerow et al.*, 1998, 2000]. The TRMM product 2B31 provides rainfall estimates on a ~4 × 6 km$^2$ pixel size between 36°N and 36°S (TRMM product 2B31, algorithm V6, more information available at: http://disc.sci.gsfc.nasa.gov/precipitation/documentation/TRMM_README/TRMM_2B31_readme.shtml). The TRMM 2B31 data product is a combined rainfall profile product from the Precipitation Radar (PR) and TRMM Microwave Imager (TMI). We processed these data for 10 consecutive years from 1998 to 2007 with a total of 57,718 orbits (~16 each day) and interpolated the orbital data onto an equally spaced 5 × 5 km$^2$ grid. In August 2001, the orbital boost maneuver to extend the lifetime of the TRMM platform resulted in a change of the horizontal footprint resolution to ~5.0 km. (See the auxiliary material for a more complete description of data processing and error estimations.) For Himalayan-Tibetan areas lying north of 36°N, we used the TRMM product 3B42 that includes data from the Special Sensor Microwave/Imager, the Advanced Microwave Scanning Radiometer, and the Advanced Microwave Sounding Unit to estimate precipitation at a spatial scale of 0.25 × 0.25° (~30 × 30 km) [*Huffman et al.*, 2007].

[7] The instantaneous rainfall amounts (mm/hr) were converted (or calibrated) to mean seasonal or annual rainfall (m/yr) with daily and monthly, ground-based rainfall measurements from the greater Himalaya realm (n = 1741, see Figure 1b for location and Figures 2 and S3 for calibrations as well as the auxiliary material for more information) [*Barros et al.*, 2000; *Bookhagen and Burbank*, 2006; *Easterling et al.*, 2002]. Generally, the data reveal robust and consistent results, even though the stations span >10° in latitude, >30° in longitude, and an elevation range from sea level to 4.5 km asl (Figures 1b and 2 and S2). Most of the heavy rainfall occurs below 4 km [*Barros et al.*, 2000; *Bookhagen and Burbank*, 2006; *Parthasarathy et al.*, 1992] and almost none above 6 km [*Harper and Humphrey*, 2003]. We used the rainfall data sets to calculate the river flow from the upstream drainage area using the 90-m flow-routing grid derived from the patched topographic data [*Tarboton et al.*, 1991]. We have routed the flow both monthly and annually.

[8] Our rainfall calibration parameters that convert rainfall intensities to mean annual rainfall are very similar to those from a similar study in the Andes of South America with nearly 2000 gauge stations [*Bookhagen and Strecker*, 2008]. In general, the remotely sensed rainfall data correlate well with the ground-control stations; even high annual-rainfall amounts above 5 m/yr are accurately depicted (Figures 2 and S2). We have performed several calibration routines in which we included only rain-gauge stations from below 0.5 km asl (n = 1398) or from above 0.5 km (n = 343) and their respective conversion factors differ only by ~6%. In this study, we rely on conversions factors between instantaneous and seasonal or annual rainfall (mm/hr to m/yr) based on all station data (Figure 2). This corroborates our earlier findings from the Himalaya indicating that, despite non-continuous TRMM-rainfall data series, relative values represent a valid rainfall distribution [*Bookhagen and Burbank*, 2006].

[9] We summarize here the additional steps we took to improve our previous rainfall estimates [*Bookhagen and Burbank*, 2006]: (1) bilinear interpolation of every orbit of the TRMM 2B31 RRSurf product onto an equally spaced grid to homogenize the data (this includes a correction for pre- and post-boost orbits), (2) calibration with 1741 ground-control stations to create a robust calibration factor for conversion from instantaneous rainfall rates measured in mm/hr to mean annual or seasonal rainfall amounts (m/yr), and (3) inclusion of error estimations for satellite and rain-gauge measurements to provide precision boundaries.

[10] In a separate calibration effort to convert instantaneous rainfall amounts (mm/hr) to mean seasonal or mean annual amounts (m/yr), we have analyzed data from the 46-day TRMM cycle. This conversion method was previously used by researchers for estimating Himalayan rainfall using a Precipitation Radar product (TRMM 2A25) [*Anders et al.*, 2006; *Finnegan et al.*, 2005]. Except for being in the same position at the same time at the start of each cycle, the satellite's orbit samples each location at different times of day during a cycle [*Kummerow et al.*, 1998]. It has been argued that by dividing each year into approximately eight 46-day periods, an even sampling of the diurnal cycle is

[1]Auxiliary materials are available in the HTML. doi:10.1029/2009JF001426.

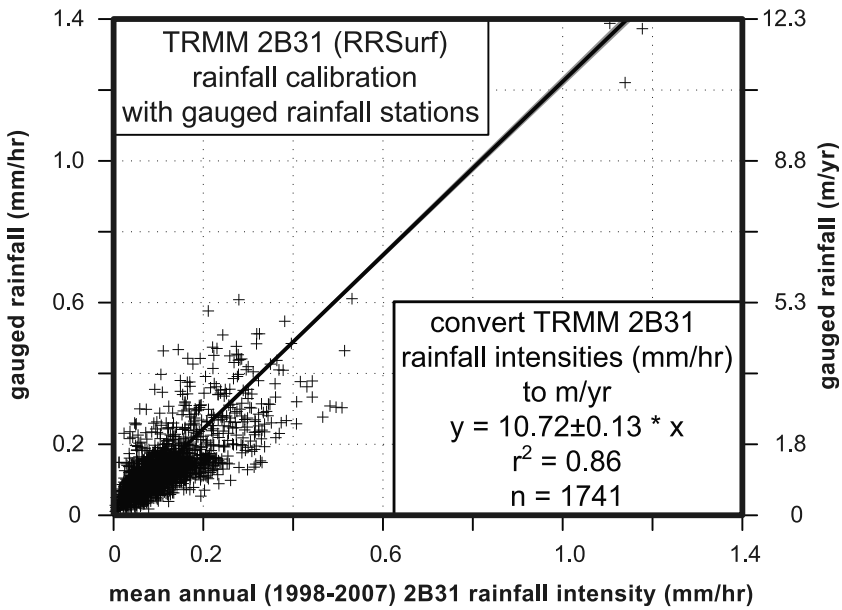


**Figure 2.** Calibration of 10-year mean annual TRMM 2B31 data with 1741 stations throughout the Himalaya and foreland (see Figure 1b for locations). Rainfall intensities are linearly related with gauged rainfall over more than an order of magnitude (y = 10.72 ± 0.13*x; ± 95% confidence interval). TRMM2B31 values are weighted with RMS estimates from TRMM product 2B31 (Sigma-RR-Surf). High-amount rainfall stations (>10 m/yr) are from south of the Shillong Plateau. For statistical rigor, we have performed the same calibration with high rainfall intensities (>6 m/yr) removed; the predictive relation remains statistically identical. The ordinate displays mean annual-rainfall intensity for each rainfall-station pixel and was derived from TRMM product 2B31 (RR-Surf).

produced [*Anders et al.*, 2006; *Kummerow et al.*, 1998]. The average rain rate within each period is then multiplied by its length to estimate the rainfall amounts [*Anders et al.*, 2006; *Kummerow et al.*, 1998]. The sum of eight periods results in the mean annual rainfall. We compare this conversion scheme to the rain-gauge data and find that, although it yields a strong correlation ($r^2 = 0.87$), it overpredicts observed absolute rainfall by ~45% (Figure S3). Furthermore, this simplified calibration scheme with 8 values per year results in mean annual rainfall rates only and does not allow analysis at a higher temporal (seasonal) resolution.

### 2.3. TRMM Lightning Image Sensor

[11] We used the Lightning Imaging Sensor (LIS) onboard the TRMM satellite to determine the distribution and variability of lightning (cloud-to-cloud, intracloud, and cloud-to-ground lightning) at the same time as rainfall measurements were made [*Christian et al.*, 1999]. (See the auxiliary material for a more complete description.) The LIS represents a significant advance over any previous satellite-borne lightning detector. LIS observations can be readily associated with the thunderstorms that produced them. The detection of even a single lightning discharge is significant and provides important information bearing on storm location, rainfall estimates, storm height, the presence of ice, and lightning frequency [e.g., *Petersen and Rutledge*, 2001].

### 2.4. Evapotranspiration

[12] We have used a global evapotranspiration algorithm based on MODIS and global meteorology data described by *Cleugh et al.* [2007], *Mu et al.* [2007], and *Sun et al.* [2007]. This algorithm is based on the Penman-Monteith method and considers both the surface energy partitioning process and environmental constraints on evapotranspiration [*Cleugh et al.*, 2007; *Monteith*, 1964]. The improved algorithm developed by *Mu et al.* [2007] was evaluated with 19 AmeriFlux eddy covariance flux towers and shows a strong ($r^2 = 0.76$) correlation with the field data. (See the auxiliary material for a more complete description of data processing.) For the western Himalaya, we have compared basin-average evapotranspiration estimates derived from the MODIS algorithm with in situ field measurements [*Singh et al.*, 1997] and find good agreement.

### 2.5. Snow-Cover Area, Surface Temperature, and Solar Radiation

[13] We have used data from the Moderate Resolution Imaging Spectroradiometer (MODIS) to quantify snow cover (MOD10) and surface temperature (MOD11) [*Hall et al.*, 2002; *Hall and Casey*, 2003; *Wan et al.*, 2004; *Wan and Dozier*, 1996; *Wan et al.*, 2002]. (See the auxiliary material for a more complete description of data processing.) The MOD10C2 product yields pixel values indicating the percentage of snow cover within a 0.05 × 0.05° (~6 × 6 km) grid cell over an 8-day period. With these values, we calculate mean monthly snow-cover areas from 2000 to 2008.

[14] To estimate land surface temperature, we have used the MODIS land surface temperature observations (MOD11C2) that are collected at the same spatial scale as the snow-cover data [*Wan et al.*, 2004]. These temperature data are then used to calculate the days with a mean temperature above freezing.

[15] We have calculated mean monthly solar radiation for each 1 × 1 km grid cell from our DEM using an approach described by *Kumar et al.* [1997]. This method calculates the clear-sky radiation corrected for the incident angle, plus both diffuse and reflected radiation. This total radiation correction can be significant, because the steep terrain results in considerable self-shading. Insolation depends on time of year and day, latitude, elevation, slope, and aspect. We first calculate hourly solar radiation and then derive a mean monthly amount from this.

### 2.6. Parameterization of the Snowmelt Model

[16] In general, runoff modeling is concerned with the transformation of incoming precipitation to outgoing streamflow, while taking into account losses to the atmosphere, temporary storage, and both lag and attenuation as water is routed by fast and slow pathways above and below the ground. When precipitation falls as snow, rather than rain, a snowpack accumulates until warmer weather allows melting. Meltwater is routed by the same pathways as rainfall, so most snowmelt models are rainfall-runoff models with extra routines added to store and subsequently melt precipitation that falls as snow. Several related semi-empirical approaches quantify lag times, transient storage of moisture in mountainous catchments, and conversion of snow into snow-water equivalents, including the Soil and Water Assessment Tool (SWAT) model [e.g., *Arnold and Fohrer*, 2005], the degree-day method [e.g., *Hock*, 2003; *Linsley*, 1943; *Rango and Martinec*, 1995], the snowmelt-runoff model [e.g., *Brubaker et al.*, 1996], and snow accumulation and ablation models using the physics of snow-cover energy exchange [e.g., *Anderson*, 1973; *Franz et al.*, 2008]. Despite some of the models' simplicity, they generally perform well when predicting discharges in snow-covered mountainous terrain [e.g., *Ferguson*, 1999; *Hock*, 2003; *Immerzeel et al.*, 2009; *Rango and Martinec*, 1995].

[17] We have employed a modified snowmelt runoff model (SRM) that uses solar radiation and temperature to convert snow-covered areas into a meltwater runoff component. The radiation term is important in low latitude, high-elevation mountain belts because high solar radiation causes meltwater generation at temperatures below the freezing level. The snowmelt $S_{melt}$ is calculated using the following relation:

$$S_{melt} = m_Q * R + a_r * T \tag{1}$$

where $m_Q$ is the physical constant converting energy to water mass or depth (0.026 cm $W^{-1}$ $m^2$ $day^{-1}$), $R$ is the incident solar radiation, $a_r$ is a restricted degree-day factor (cm $°C^{-1}$ $day^{-1}$), and $T$ the mean daily temperature (°C). We have followed *Rango and Martinec* [1995] and modified the equation (1) to reflect the number of degree days above 0°C taken from the MODIS land surface temperature data and (2) to include the per-pixel snow-covered area derived from the MODIS Snow-Cover data. Our approach has then been applied to 1 × 1 km pixels, a spatial-resolution compromise between data availability and steep climatic gradients in the Himalaya. We have limited our analysis to mean-monthly estimates that allow us to identify seasonal patterns on a large, regional scale. In summary, we have used the following parameterization to estimate snowmelt volume ($S_V$) and iteratively applied it to each pixel with the corresponding fractional snow cover ($A_s$), solar radiation ($R$), and days above freezing ($T_d$).

$$S_V = A_s\left(m_Q * R + a_r * T_d\right) \tag{2}$$

[18] For each month, we have used a different restricted degree-day factor ($a_r$), varying between 0.2 and 0.8 with higher values in the summer season. These values have been used for similar modeling efforts in mountainous terrain [*Martinec et al.*, 2007; *Rango and Martinec*, 1995] and are intended to capture the observed seasonal variability, i.e., more melting during summer months for the same mean temperature mostly due to snow-density changes. Our approach differs from previous approaches in that we explicitly model each pixel separately instead of dividing the catchment into regions with similar climatic characteristics [e.g., *Immerzeel et al.*, 2009; *Martinec et al.*, 2007]. The satellite-derived temperature, snow cover, and solar-radiation data allow us to generate spatially continuous measurements without the need to interpolate from a sparse station network.

[19] In a final step, we combine our mean-monthly TRMM rainfall data with the snowmelt model and evapotranspiration data to estimate discharges. We assume a combined rainfall and snowfall-runoff coefficient of 0.7, based on previous studies in the Himalaya [e.g., *Rao et al.*, 1996; *Hasnain*, 1999; *Singh et al.*, 1997]. We validate our modeled discharge data with a daily river-gauging network spanning the entire Himalaya (see Figure 1a for location). In general, our monthly predicted discharges match measurements within 10% (Figures 3 and S4). Importantly, runoff derived only from rainfall amounts underpredicts discharge on average by ~40%.

## 3. Study Area and Climatic Background

[20] Generally, two independent climatic regimes dominate the Himalaya domain: the monsoon system and the westerlies. The monsoon system is generally divided into the East Asian and Indian monsoon systems; these systems strongly interact and influence each other. For a more complete description of the complex relationships between vertically integrated atmospheric temperature, pressure, and rainfall content, we refer to *Webster* [1987], *Webster et al.* [1998], *Gadgil et al.* [2003], and *Wang* [2006] and to *Ding and Chan* [2005] for an overview of the East Asian monsoon. However, in order to understand the spatiotemporal precipitation variations in the Himalaya domain, especially the importance of its seasonal impacts, a basic knowledge of the two general circulation patterns is essential.

[21] The height and extent of the Tibetan Plateau and High Himalaya impose a significant barrier to atmospheric circulation patterns. For the past decades, several authors have argued that the strength of the South Asian monsoon is related to the high solar insolation on the Tibetan Plateau during the summer time [*Barros et al.*, 2004; *Bookhagen et al.*, 2005b; *Flohn*, 1957; *Gadgil et al.*, 2003; *Webster*, 1987]. In their models, during summer, the highly elevated, solar-heated Tibetan Plateau develops a near surface, low-

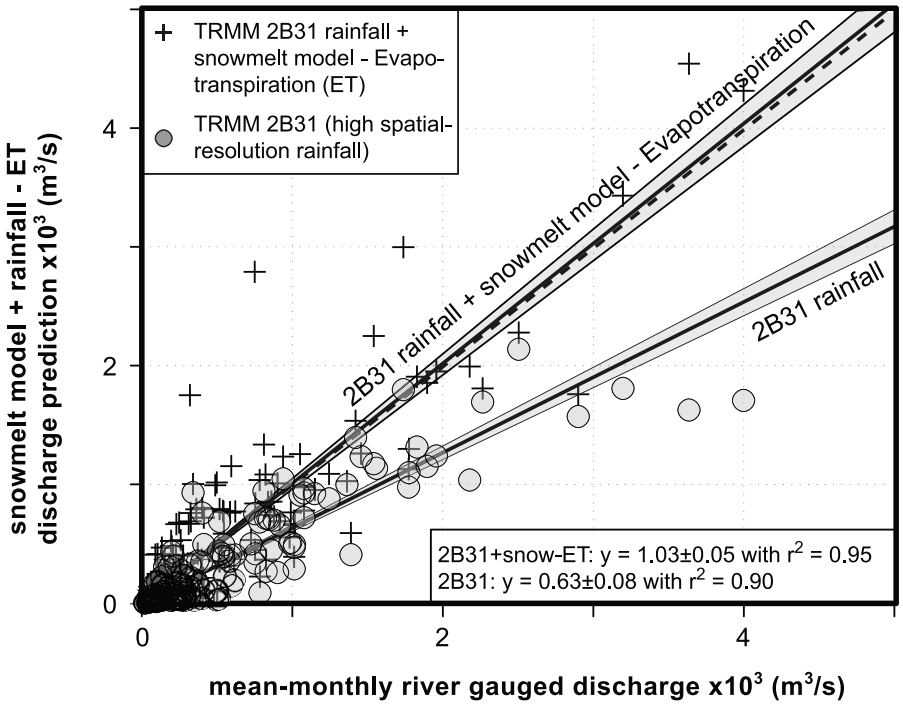


**Figure 3.** Validation results of discharges derived from rainfall, snowmelt modeling, and evapotranspiration. We have used 13 stations that recorded daily discharge amounts during our modeling period (2000 to 2007) throughout the Himalaya. We show measured mean-monthly discharge (n = 12 months × 13 stations = 156) versus error weighted mean-monthly model outputs. Shading indicates the 95% confidence intervals for the linear regression. The Nash-Sutcliffe coefficients are between 0.7 and 0.9 with a mean at 0.82 for the 13 control stations. The bold, dashed line indicates a 1:1 relation. On average, our weighted fit of the runoff model slightly overpredicts discharge amounts by ~3 ± 5%. The TRMM 2B31 rainfall (without a snowmelt and evapotranspiration component) underpredicts discharge on average by ~40 ± 8% (with values of 60% and more during the summer months). Locations of river-gauge stations are shown in Figure 1a.

pressure cell, causing the atmosphere to re-arrange its circulation patterns, which ultimately leads to strong near-surface winds in the region surrounding the plateau [the word monsoon is derived from the Arabic word for season and is used to delineate the wind-direction reversal during this time]. However, other previous and recent studies argue that the high orographic barrier produces a strong monsoon by insulating warm, moist air over continental India from the cold and dry northern latitudes [e.g., *Boos and Kuang*, 2010]. One of the main driving forces of the monsoon at its onset stage is the temperature gradient between the warm land and cooler ocean. Latent-heat release via condensation over the Indian continent contributes significantly to maintain this temperate gradient during the active part of the monsoon season [e.g., *Fasullo and Webster*, 2003; *Magagi and Barros*, 2004; *Riehl*, 1959; *Webster*, 1983].

[22] During the summer months, the thermal field of the Tibetan Plateau and the resulting strong pressure gradient modify the primary westerly winds that are characteristic of these latitudes to a southeasterly wind system in northeastern India and the realm of the Bay of Bengal [*Flohn*, 1957; *Hahn and Manabe*, 1975]. Thus, the precipitation source during the Indian Summer Monsoon (ISM) for the eastern and central southern Himalayan front is the Bay of Bengal, where monsoonal vortices are formed and move to the north and northwest [*Bookhagen et al.*, 2005b; *Lang and Barros*, 2002]. These vortexes are released during the active phase of the monsoon and initiate heavy orographic rainfall when colliding with the mountain front [*Barros et al.*, 2004; *Bookhagen and Burbank*, 2006; *Galewsky*, 2009]. Overall, the cumulative effect of all vortexes during the active phase of the monsoon results in generally wetter regions in Bangladesh, eastern India, and the central and eastern Ganges plains (Figures 4a and 5). The influence of ISM rainfall (and thus the influence of individual vortexes) decreases rapidly west of ~77°E in the vicinity of the Sutlej Valley and Garhwal Mountains [*Barros et al.*, 2004; *Bookhagen et al.*, 2005b; *Bookhagen and Burbank*, 2006]. In this western region, rainfall is dominated again by westerly and southwesterly wind systems with water vapor originating from the Arabian Sea and possibly as far away as the Mediterranean [*Barros et al.*, 2006; *Hatwar et al.*, 2005] (Figures 4 and 5).

[23] During the winter months, the temperature gradient reverses with abnormally cold areas on the Tibetan Plateau versus the warmer surrounding oceans. At this time, a pressure gradient develops that results in general northeastern wind systems [*Wang*, 2006]. However, the overall weaker

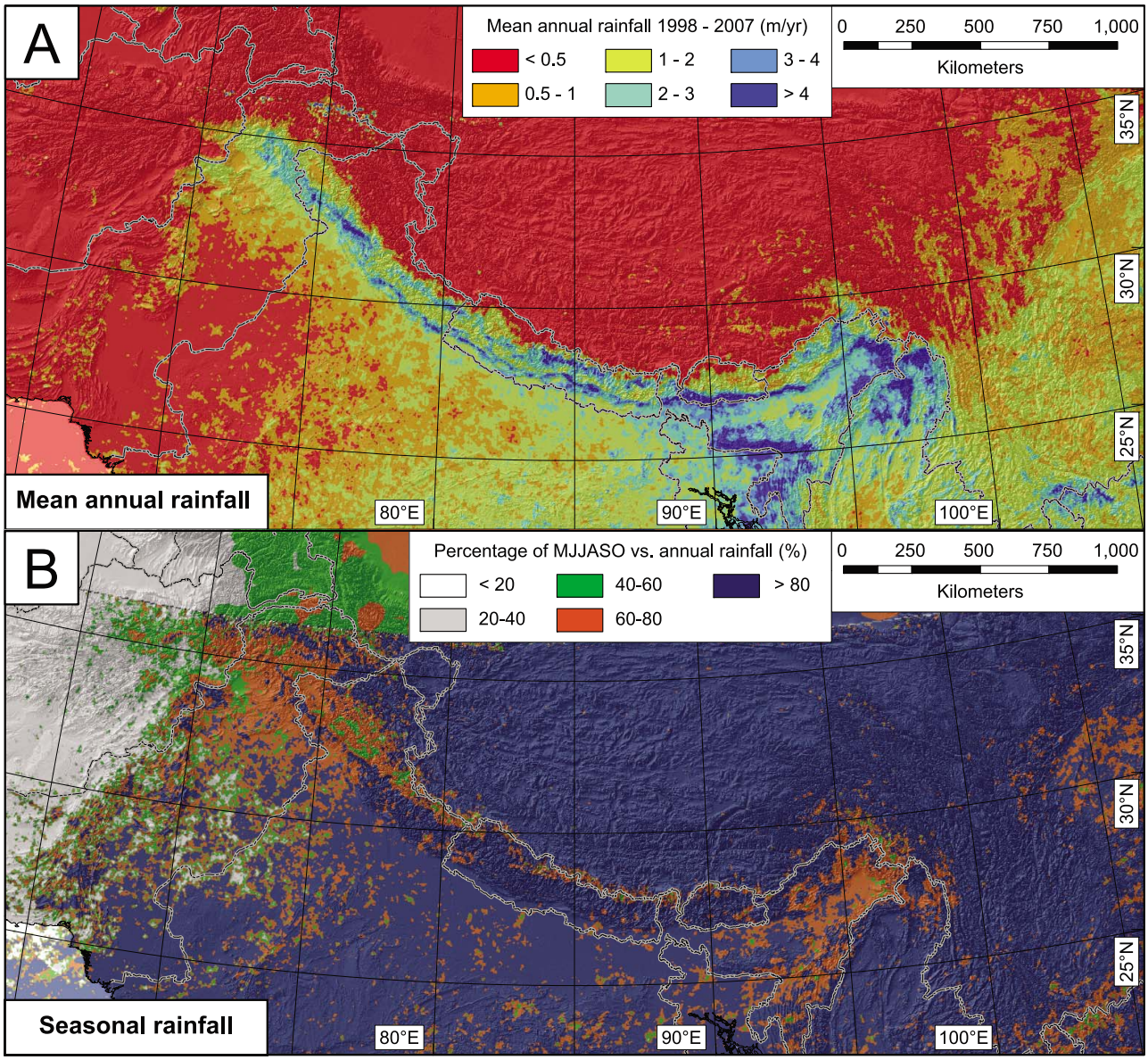


**Figure 4.** (a) Mean annual rainfall based on calibrated TRMM 2B31 data and averaged over 10 years from 1998 to 2007. Note the formation of an outer and inner rainfall band at the main topographic barriers of the Himalaya. (b) Percentage of summer rainfall (May to October) versus annual rainfall. Most Himalayan and Tibetan areas receive more than 80% of their annual rainfall during the months from May to October (blue). Only the syntaxes and western Himalaya receive significant rainfall amounts during the remainder of the year (November to April). Note the artifactual effect where the two rainfall data sets (TRMM 2B31 and 3B42) are merged at 36°N latitude (see text for explanation).

monsoon-related circulation patterns allow the influence of other synoptic circulation systems. In the Himalayan regions of northwest India and Pakistan, the Western Disturbances are the primary weather system responsible for wintertime rainfall and are westerly upper-tropospheric synoptic-scale waves [e.g., *Barros et al.*, 2006; *Dimri*, 2006; *Hatwar et al.*, 2005; *Lang and Barros*, 2004; *Wang*, 2006]. These waves are trapped and intensified by the large-scale topographic features, most notably the notch formed by the Himalaya and Hindu Kush mountains in the western syntaxis and the Himalaya and Burmese mountains in the eastern syntax. Thus, the overall rainfall distribution during the winter season significantly changes, and both Himalayan syntaxes receive more precipitation from winter disturbances than the central parts along the Himalayan front (Figure 5b).

[24] Generally, the northward push of water vapor is limited by the High Himalayan mountain chain with peaks above 7 km, although some precipitation migrates up large Transhimalayan river valleys onto the Tibetan Plateau. Orographic barriers of the Lesser and Higher Himalaya result in a precipitation-soaked Himalaya, while the regions north of the orographic barriers receive little precipitation (Figure 4a)

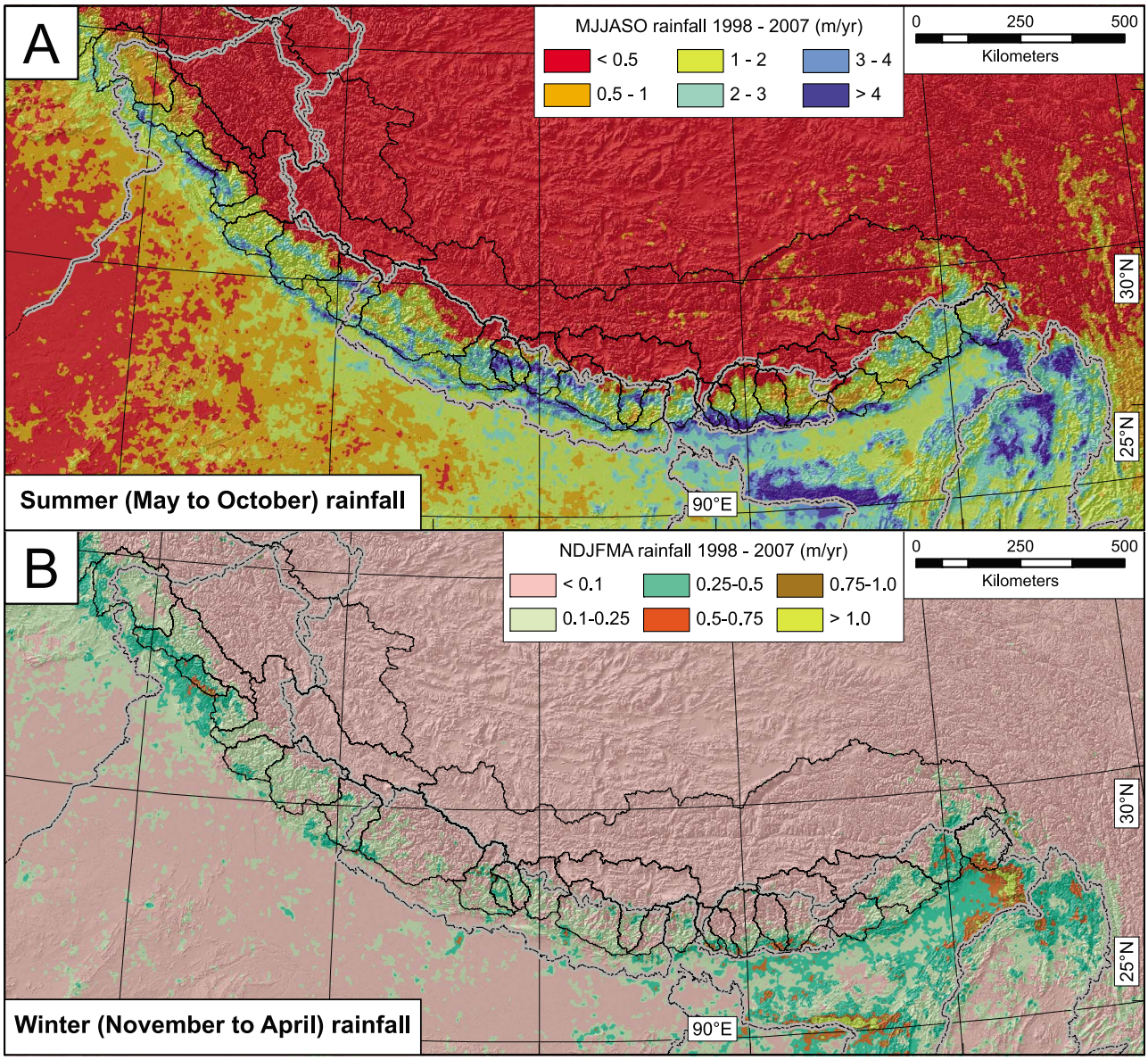


**Figure 5.** Seasonal rainfall during the Indian Summer Monsoon from (a) May to October and (b) during the winter season (November to April). Note the different scales used for the rainfall amounts; color of the highest winter rainfall match intermediate (1–2 m/yr) summer rainfall amounts. Rainfall during the summer season shows a pronounced east-west gradient in the Ganges plain, with higher amounts (>4 m/yr) occurring at the topographic barriers. The two-peak rainfall belt primarily develops during the summer season. In contrast, rainfall distribution during the winter season indicates that primarily the syntaxes receive rainfall through large-scale circulation patterns.

[*Barros et al.*, 2006, 2004; *Bookhagen and Burbank*, 2006; *Galewsky*, 2009].

## 4. Results

### 4.1. Rainfall

[25] In general, two pronounced rainfall gradients dominate the Ganges Plains and Himalaya (Figure 4a): (1) a ~6-fold east-to-west rainfall gradient with high rainfall amounts in the eastern region, closer to the precipitation source of the Bay of Bengal, and (2) a ~10-fold south-to-north rainfall gradient across the Himalayan mountains that has been previously explored [*Bookhagen and Burbank*, 2006]. The development of these characteristic rainfall belts occurs during the summer monsoon (Figure 5a). The first, outer rainfall peak occurs along the southern margin of the Lesser Himalaya within a narrow band of mean elevation (0.9 ± 0.4 km) and of mean relief (1.2 ± 0.2 km, measured within a 5-km radius) [*Bookhagen and Burbank*, 2006]. The second, discontinuous, inner band typically occurs along the southern flank of the Greater Himalaya (elevation and relief: both 2.1 ± 0.3 km) [*Bookhagen and Burbank*, 2006].

[26] Both rainfall gradients are clearly expressed on the regional, annual-rainfall map (Figure 4a). The summer monsoon period from May to October (6 months) is responsible for >80% of annual rainfall in the Greater Himalaya and Tibetan region (Figure 4b). A slightly lower ratio pertains if the "monsoon" is restricted to the months of June to September (4 months versus 6). Because monsoonal rainfall in the far eastern Himalaya starts earlier and ends later, we include the months of May and October in our calculation. Only the eastern and western syntaxes receive significant amounts of rainfall during the winter season (Figures 4b and 5b).

[27] In order to quantify and explore large-scale rainfall patterns, we analyzed a ~400-km-wide and 2500-km-long swath along strike of the Himalaya (Figure 6a) and projected the data onto a straight line. We separated the data both spatially by elevation and temporally by season. When topographically divided, the annual rainfall data reveal a ~6-fold east-to-west rainfall gradient in the Ganges foreland for elevations ≤500 m asl (Figure 6b). The highest volume of rainfall occurs in the eastern regions, closer to the precipitation source: the Bay of Bengal. The western regions of the foreland lie beyond the monsoonal conveyer belt. This distinct rainfall gradient along the foreland lies in striking contrast to rainfall patterns in higher elevations between 500 and 5000 m asl in at least two respects (Figures 6b and 6c). First, integrated rainfall volumes from orogen-perpendicular swaths in the mountainous regions are ~5 times lower than total amounts on the eastern plains at elevations <500 m, but become nearly equivalent in the western regions, despite the fact that the highest rainfall rates generally occur in elevated terrain [*Bookhagen and Burbank*, 2006]. Second, our data reveal no significant rainfall gradient along strike within the Himalaya (elevations ≥ 500 m: Figures 6b and 6c). Instead, this contrast with rainfall in the foreland emphasizes the different processes leading to rainfall in the mountainous regions: rainfall in the Himalaya responds to orographic controls, whereas rainfall in the foreland is a function of distance from the Bay of Bengal. The integrated rainfall amount in the mountains appears strikingly similar for at least ~1000 km along strike.

[28] When separated by season, the rainfall distribution reveals that the strong east-west rainfall gradient in the plains is a summer phenomenon. During the winter season, higher amounts of rainfall-water volume occur primarily in the eastern and western syntaxes and at higher elevations (dashed black lines in Figure 6c).

[29] In order to characterize the orographic impact on rainfall distribution, we have extracted fifty 50-km-wide by 300-km-long swaths along the Himalaya (Figure 7a). All swath profiles trend perpendicular to the mountain front: an orientation parallel to our assumed atmospheric transport direction. This parameterization is not entirely correct for all places, because water-vapor supply depends on individual storm tracks that are not always perpendicular to the mountain front [*Barros et al.*, 2004]. Major river valleys are (sub-) parallel to our swath profiles, however, and they funnel water vapor and rainfall into the interior, high-elevation parts of the Himalaya.

[30] We identified two intrinsic end-members of topographic profiles in the Himalaya: (1) in far western and eastern parts of the Himalaya, 50-km-wide swaths reveal that the mean topography rises more or less steadily to an average elevation of 5 km, and relief increases rapidly to amounts above 3 km (Figure 7b); (2) in contrast, particularly in the central and central-western Himalaya, mean topographic profiles are characterized by a two-step morphology of which the outer step corresponds to the Lesser Himalaya and the inner step to the Higher (Greater) Himalaya geologic units (Figure 7c). These two classes of topographic profiles are mimicked by the rainfall distribution, with a single, high peak of up to 6 m/yr for the steadily increasing topography versus two peaks with lower amounts of ~4 m/yr for the two-step morphology. Almost every profile can be clearly assigned to one of these two topographic classes. [These two topographic geometries are typically related to the distance of the Main Central Thrust, MCT, from the southern Himalayan mountain front.] Importantly, whereas the position and magnitude of the rainfall peaks varies among swaths during transport of water vapor and rainfall propagation into the orogen, the integrated rainfall amount within the mountains remains strikingly similar along strike of the Himalaya (Figure 6b).

### 4.2. Rainfall Intensities and Lightning Strikes

[31] In order to compare storm strength along the Himalaya, we have extracted the maximum rainfall intensity measured in mm/hr during the 10-year measurement period (Figure 8a). Rainfall intensities do not mimic mean rainfall distributions (Figure 9): whereas mean annual rainfall varies significantly along strike (Figure 7b), rainfall intensities are more similar along strike (Figure 9). Overall, maximum rainfall intensities during the 10-year measurement period are on the order of 60–80 mm/hr in all frontal and low-elevation regions of the Himalaya (Figures 8 and 9). Rainfall intensities associated with the inner rainfall peak at medium elevations in the central Himalaya are somewhat lower: on the order of 40–60 mm/hr (Figure 9). Interestingly, peak rainfall intensities in the central and in the eastern Himalaya are shifted several dozen kilometers northward compared to mean annual rainfall amounts. This shift most likely reflects propagating storm events and is associated with high-intensity storms that trigger hillslope-erosion processes such as debris flows and landsliding.

[32] Despite the generally uniform mean annual rainfall along strike (Figure 6b), rainfall intensities in the western and eastern Himalaya associated with a single rainfall peak are 15–30% higher (70–80 mm/hr) than in the central Himalaya (~60 mm/hr), whereas intensities are still lower (~40 mm/hr) within the Nepalese Himalaya at the second, more northerly, high-rainfall band. Importantly, the largest area of high rainfall intensity is in the low-elevation, frontal western Himalaya (Figure 9a).

[33] The analysis of the TRMM Lightning Image Sensor (LIS) reveals >10-fold variation in the number of flashes per $km^2$ per year along strike of the Himalaya (Figure 8b). We use these data as an additional proxy for rain-storm strength because heavy lightning indicates strong convection in an unstable atmosphere. Regions with increased lightning activity are more likely to have intensified convection resulting in more violent rainstorms [e.g., *Petersen and Rutledge*, 2001]. Previously, *Barros et al.* [2004] identified the regions of northern India and Pakistan with high lightning amounts. Similarly, *Houze et al.* [2007] describe the western Hima-

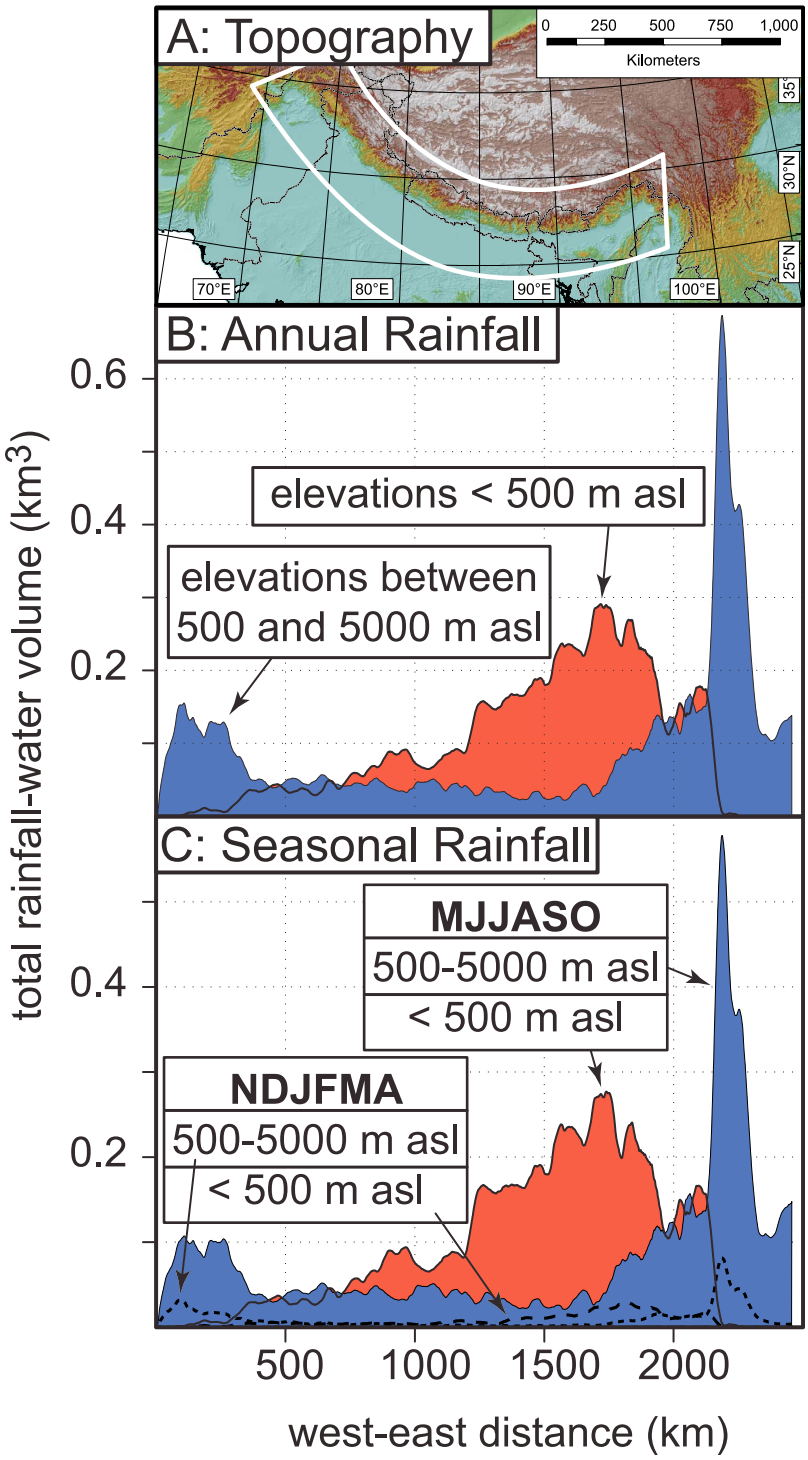


**Figure 6.** (a) Location map of the 400-km-wide, 2500-km-long rainfall swath following the Himalayan arc. All topographic and climatic data have been projected onto a straight line. (b) Annual rainfall amounts in all areas with (1) elevations <500 m (i.e., the Ganges Plain) and (2) elevations between 500 and 5000 m asl (i.e., the mountainous Himalaya). Note the strong east-west gradient on the Ganges Plain (elevations < 500 m asl) and high rainfall amounts in the eastern Himalaya, closer to the Bay of Bengal moisture source. Despite the strong rainfall gradient along the foreland, areas at elevations >500 m receive a nearly constant water volume between 400 and 1800 km along-strike. (c) Seasonal rainfall, where black dashed lines outline the winter season (November to April) rainfall. During winter, the slight increase in rainfall-water volume in the eastern and western area reflects winter storms that drive rainfall into the higher elevation areas. The greatest overall rainfall amounts in the higher elevated, eastern Himalaya are related to the Shillong Plateau.

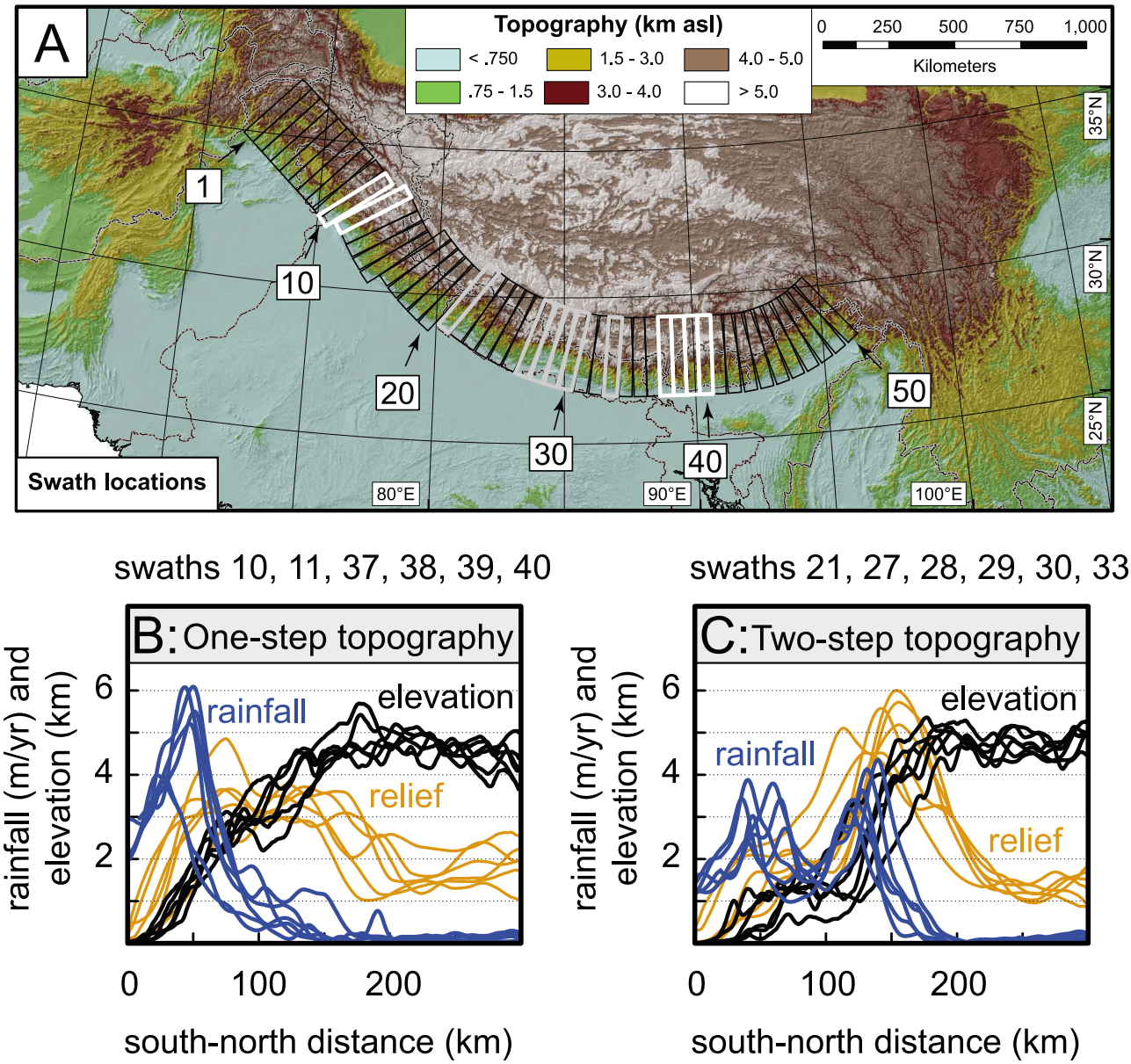


**Figure 7.** (a) Location of numbered 50-km wide and 300-km long swaths used to illustrate two topographic, relief, and rainfall-distribution end-members. (b) Steadily rising topographic profile results in a single high-amount rainfall peak (swaths used are those shown by white polygons in Figure 7a). A 5-km-radius relief is indicated by the orange lines. (c) Two-step morphology coinciding with the Lesser Himalaya units and Higher (Greater) Himalaya forming two rainfall peaks (swaths are gray polygons in Figure 7a).

laya as a region with deep convection processes. We support their findings and also identify high lightning amounts in the Marsyandi catchment in central Nepal, in the eastern Himalaya, and to the south of the Shillong Plateau (Figure 8b). The abnormally high amounts in central Nepal are in fact the highest lightning rates within the Higher Himalaya – all other elevated flash rates are located at or near the southernmost Himalayan topographic front. A generally good spatial correlation exists between high rainfall intensities and high lightning rates (Figures 8a and 8b).

[34] TRMM-derived lightning rates indicate a steep west-to-east gradient with highest lightning amounts in the western regions in all elevation slices (Figures 9). On average, lightning rates in the western Himalaya are twice as high as in the central and eastern Himalaya. No significant lightning rates are recorded at elevations above 4 km. Overall, these data suggest a steep, along-strike gradient with generally more violent storms in the west than in the central and eastern Himalaya (Figures 8b and 9). Thus, despite the overall decrease in monsoonal rainfall amount toward the west (Figures 4a and 6b), a westward increase in the apparent intensity of convection and storm strength leads to broad spatial uniformity in maximum rainfall intensity for the frontal, outer rainfall peak (Figure 9).

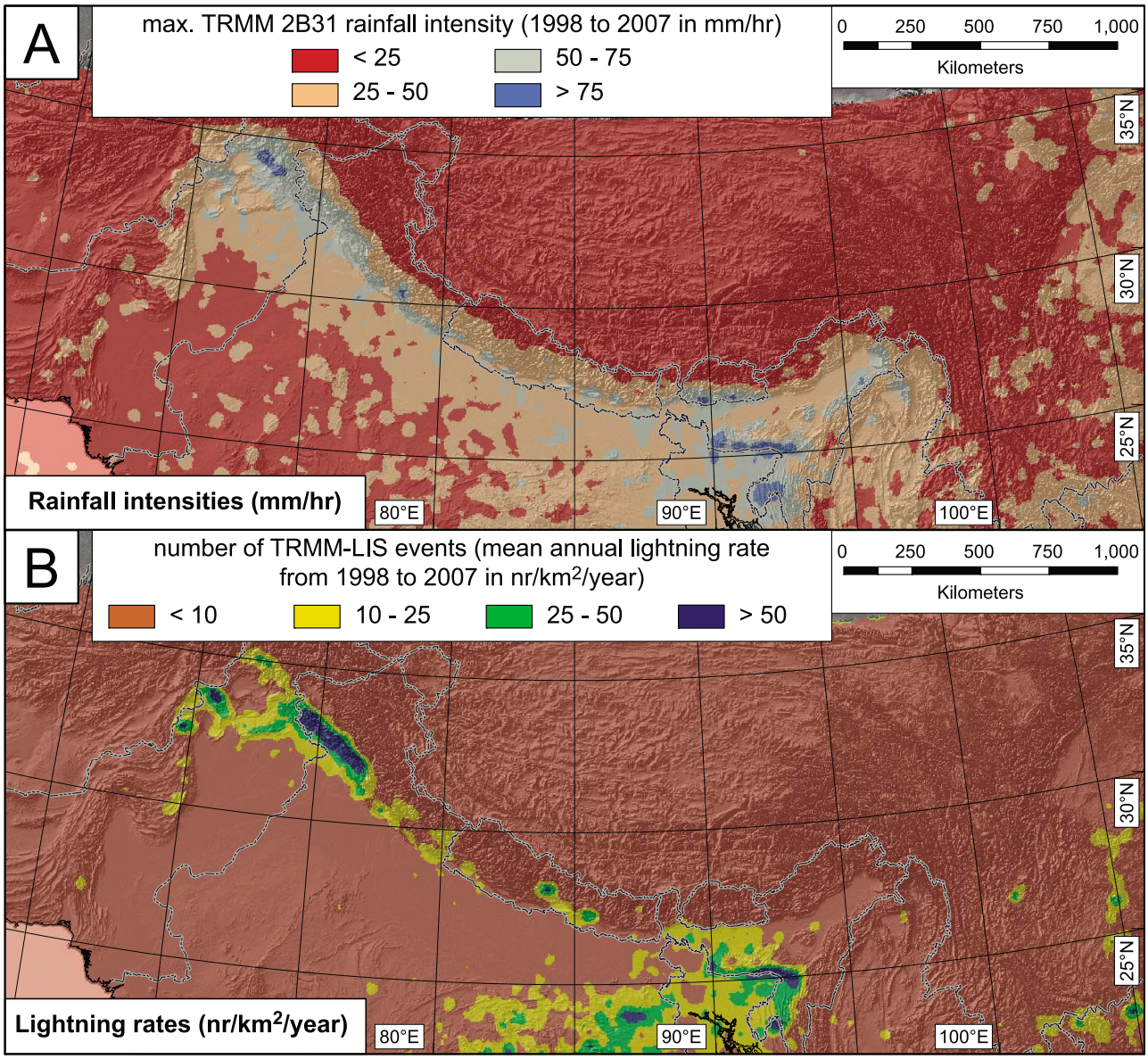


**Figure 8.** (a) Maximum rainfall intensity (mm/hr) during the 10-year measurement period. (b) TRMM LIS (Lightning Image Sensor) mean annual lightning rates, averaged over the same time period. Both data sets were smoothed by a 25 × 25 km$^2$ (5 pixel) window. Generally, high rainfall intensities correlate with orographic barriers, but the western (NW India, Pakistan) and eastern Himalaya (Bhutan, Shillong Plateau) experience significantly higher intensities than the central Himalaya. These high-intensity areas are prone to flash floods. The high lightning rates in these western and eastern areas underline the unstable atmospheric conditions. Within the central Himalaya, moderate to high lightning amounts are recorded only in central Nepal.

**Figure 9.** Smoothed rainfall, topography, rainfall intensity and number of lightning events averaged over several swaths for the (a) western, (b) central, and (c) eastern Himalaya. Bold lines with gray shading indicate mean topography and $\pm 2\sigma$ amounts, blue lines indicate TRMM-derived rainfall (both on left-hand $y$ axis). Dashed blue lines show maximum rainfall intensity during the 10-year measurement period and red, bold line indicates number of lightning events per km$^2$ per year (right-hand $y$ axis). See Figure 8 for swath locations. Note that rainfall intensities are similar between the regions despite the different mean rainfall amounts.

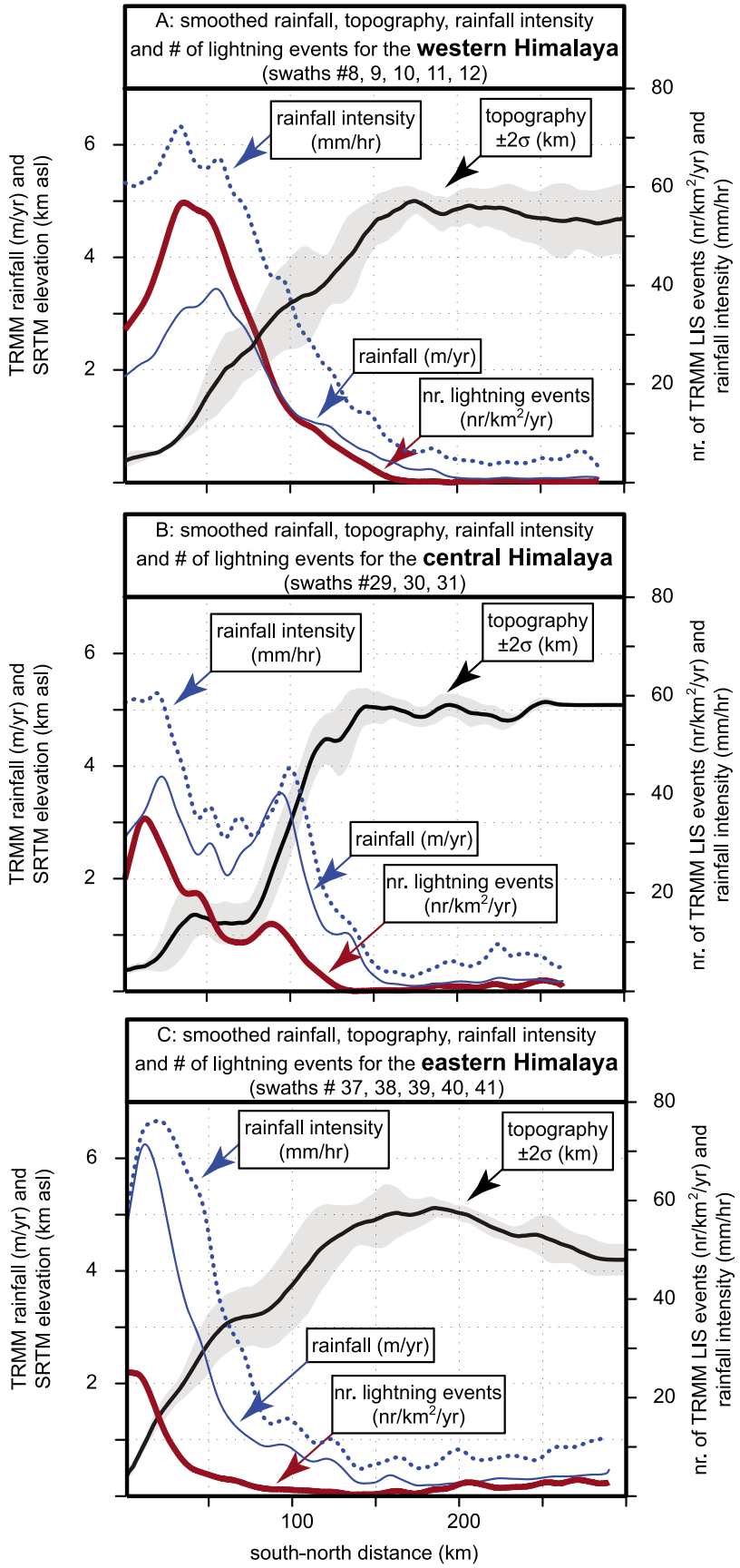
A: smoothed rainfall, topography, rainfall intensity and # of lightning events for the western Himalaya (swaths #8, 9, 10, 11, 12)
B: smoothed rainfall, topography, rainfall intensity and # of lightning events for the central Himalaya (swaths #29, 30, 31)
C: smoothed rainfall, topography, rainfall intensity and # of lightning events for the eastern Himalaya (swaths # 37, 38, 39, 40, 41)
rainfall intensity (mm/hr)
topography ±2σ (km)
rainfall (m/yr)
nr. lightning events (nr/km²/yr)
TRMM rainfall (m/yr) and SRTM elevation (km asl)
nr. of TRMM LIS events (nr/km²/yr) and rainfall intensity (mm/hr)
2
4
6
20
40
60
80
100
200
south-north distance (km)

**Figure 9**

### 4.3. River Flow: Spatiotemporal Contributions of Rainfall, Snowmelt, and Evapotranspiration

[35] In order to estimate the spatiotemporal hydrological river flows, we have created simple, but robust snowmelt and evapotranspiration models and combined them with our rainfall estimates. All data sets are based on calibrated satellite data to provide measurements for the remote Himalaya regions. Satellite-input data for our snowmelt and evapotranspiration models have weekly temporal resolutions; the critical, high-spatial resolution rainfall data are robust on monthly timescales and thus we have calculated monthly averages over the 10-year measurement period. In a second step, the three water-balance components are combined into a runoff model defined by the DEM and are accumulated to generate monthly river flows (also referred to as monthly averaged discharges). In general, the river flows calculated from the snowmelt model, evapotranspiration, and rainfall captures very well ($r^2$ = 0.95) the spatial and temporal distribution of a river-gauged network (Figure 3). The Nash-Sutcliff coefficient [*Nash and Sutcliffe*, 1970] varies between 0.7 and 0.9 for the 13 control stations, with a mean of 0.82. Importantly, the model accurately produces the snowmelt and rainfall peak for the Indus (Figure 10a) and Sutlej Rivers, each of which has a high snowmelt contribution. Here, we emphasize the discharges derived from rainfall and snowmelt contribution – evapotranspiration generally has an impact of only a few percent in the mountainous catchments (Figures 10a and 10b). Evapotranspiration becomes more important, however, in the low-elevation Himalayan foreland – a region that is not included in this study (Figure S5).

[36] Next, we explore the spatiotemporal variation of snowmelt and rainfall for each of the 27 major Himalayan catchments draining to the south (see Figure 1a for locations). As expected, discharge volumes are strongly dependent on catchment size (Table 1 and Figure 11). Interestingly, catchments in the eastern and central Himalaya receive more than ~70% of their annual rainfall during the summer monsoon, whereas catchments beyond the end of the Indian Summer monsoon conveyer belt (west of the Sutlej: catchment #6 in Figure 1, see also Figures 4 and 5a) receive high amounts of precipitation from winter westerlies as well (Figure 11). At the Himalaya's eastern end, the Tsangpo/Brahmaputra catchment has the highest discharge, whereas the second largest catchment – the Indus – has a somewhat lower discharge (Table 1).

[37] An important distinction between the Himalaya's two largest rivers is that Tsangpo discharge is primarily derived from rainfall (~80%), whereas Indus discharge has a significant snowmelt component (~66%) (Figure 11a). The third largest catchment by area – the Sutlej – in the western Himalaya, has a high snowmelt component (~57%) as well, whereas the third largest catchment by discharge – the Karnali in the central Himalaya – is largely rain-fed (~80%).

[38] On an annual timescale, snowmelt provides ~15 to 60% of discharge in the western Himalaya (Indus to Sutlej: catchments #1 to #6 in Figure 1 and Table 1), whereas the central and eastern Himalaya receive less than 20% of

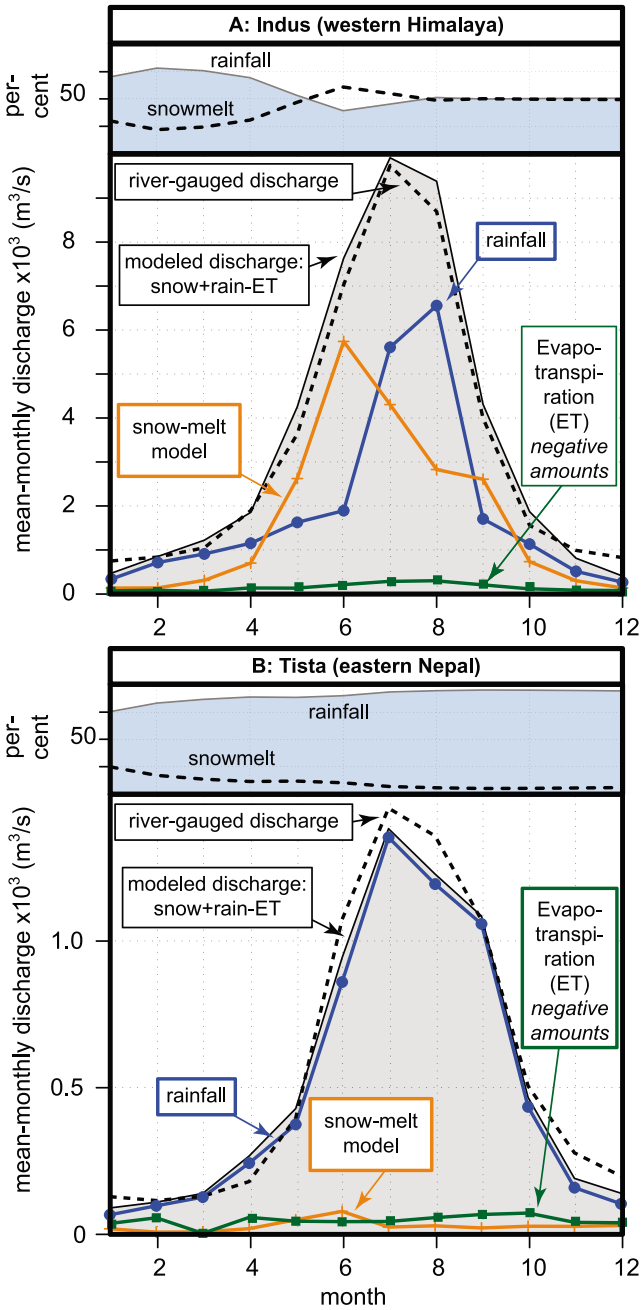


**Figure 10.** Characteristic annual hydrographs for the (a) snowmelt-dominated Indus (drainage area: ~200 × $10^3$ km$^2$, #1 in Figure 1) and (b) rain-fed Tista (~8 × $10^3$ km$^2$, #18 in Figure 1) catchments from the western and central Himalaya, respectively. Bold dashed lines indicate mean-monthly discharge measurements and shaded areas show results from modeled discharge (snowmelt plus rainfall). Blue circles indicate discharge from rainfall and orange crosses indicate snowmelt-derived discharges. Green squares show evapotranspiration (ET). Note that ET amounts are negative in the hydrologic-budget equation. Overall, the model successfully mimics the general discharge pattern with Nash-Sutcliffe coefficients of 0.88 (Indus) and 0.86 (Tista). Panel above hydrographs indicates the rain versus snow contribution in the cumulative sum. Note the temporal discrepancy in rainfall and snowmelt runoff in the Indus catchment: Discharge is dominated by snowmelt in the pre- and early monsoon season, whereas rainfall becomes more important during the mid to late summer.

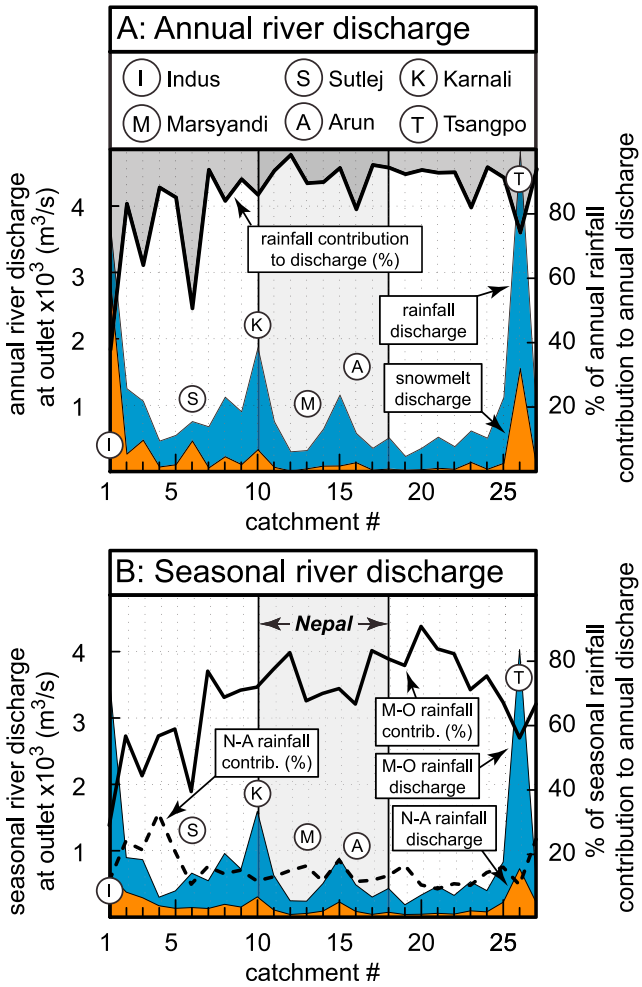


**Figure 11.** (a) Annual discharge derived from rainfall and snowmelt contributions. Discharge derived from rainfall plus snowmelt minus evapotranspiration is calculated at each catchment's outlet at the Himalayan front from west to east (see Figure 1a for catchment location and Table 1 for catchment characteristics). In all the following figures using the 27-catchment view, the gray band from catchments #10 to #18 indicates catchments within Nepal. Top panel shows rainfall-derived (blue) and snowmelt (orange) discharge. Bold line indicates percentage of rainfall contribution to annual discharge. Discharge is a function of climatic parameters and catchment size. Western catchments receive low rainfall contributions but significant snowmelt contributions. (b) Seasonal discharge distribution for the summer (May to October) and winter (November to April) season versus annual discharge. Summer rainfall in Nepalese catchments accounts for between ~60–85% of the annual discharge. Western catchments receive less than ~50% of their discharge contribution from summer rainfall.

their discharge from snowmelt (Figure 11a and Table 1). Importantly, for all Himalayan rivers draining into the Indian Ocean (the Sutlej (#6) to Indus (#1)), the snowmelt contribution is significant (Figures 11a and 13b and Table 1) due to their high winter-snow cover area and low monsoonal rains (Figure 12c). From a seasonal perspective, central and eastern Himalayan catchments receive ~60 to 85% of their annual discharge as rainfall during the summer (May to October) (Figures 11b and 13a and Table 1).

[39] The Ravi (#4), Seti (#12), and Wang (#20) catchments are the wettest along the Himalayan front (Figure 12a). However, these catchments are generally smaller and tend to be restricted to the southern, wetter flank of the Himalaya. Ignoring these river basins, spatially averaged annual rainfall rates appear to be almost uniform along the Himalaya with a slight westward-decreasing gradient and with annual averages between 1.5 and ~2.0 m/yr (Figure 12a).

[40] The seasonal snow cover derived from MODIS satellite data shows a clear, west-to-east gradient (Figure 12c). For the western half of the catchments, the mean elevation increases slightly westward. This elevational trend, when combined with the influence of winter westerlies and more northerly latitudes, results in a higher average snow cover. Interestingly, the summer snow cover shows only a gentle west-east gradient, suggesting similar snow-cover areas throughout the Himalaya.

[41] Seasonal contribution of rainfall and snowmelt to annual discharge shows three distinct characteristics (Figures 13 and 14). First, rainfall during the summer season dominates annual discharge in the central and eastern Himalaya (Figures 13b, 14, and S6d, Table 1). During the pre- and early monsoon season from May to July, more than ~35% of the annual discharge is derived from rainfall in catchments east of the Sutlej River (catchment #6 in Figure 1, Figure 13a). Overall, these catchments receive more than ~80% their annual discharge amounts as rainfall between May and October. Second, summer snowmelt dominates discharge in the western Himalaya, west of the Sutlej River (Figures 13b and S6d). For example, the Indus River catchment receives 40% (Sutlej: 27%) of its annual discharge during the 3-month period from May to July. On average, catchments west of the Sutlej receive more than 30% of their annual discharge amounts as snowmelt between May and October (Figure 13b and Table 1). In all other Himalayan catchments except for the Tsangpo/Brahmaputra, the snowmelt contribution between May and October is <15% of the annual discharge (Figure 13b and Table 1). Third, river flow in the pre- and early monsoon season from March to June includes a large snowmelt contribution, ranging from 30 to ~60% across all Himalayan catchments.

### 4.4. Testing the Validity of Discharge Predictions

[42] In an attempt to more accurately account for the influence of diverse factors on runoff, we have analyzed discharge measurements along the Sutlej Valley (western Himalaya, catchment #6 in Figure 1) [*Beas Bhakra Management Board* (*B.B.M.B.*), 2000; *Bookhagen et al.*, 2005b]. There, we have three reliable discharge sites located between the Tibetan Plateau and the southern part of the catchment (Figure 15). The higher elevation stations are most influenced by snowmelt, whereas the gauging stations in the middle Sutlej Valley are influenced by both rainfall and snowmelt; the lowest elevations have a significant rainfall component and vegetation cover that leads to generally higher evapotranspiration. For all cases, our discharge model predicts the measured discharge equally well (Figure 15) (cf. Figures S7 and S8). Importantly, our discharge model also succeeds in predicting measured snowmelt contributions from several

**Table 1.** Hydrological Overview and Summary of All 27 Major Southern Himalayan Catchments[a]

| Number | Catchment (*Country*) | Size ($km^2$) | Mean Annual 2B31 Rainfall (m/yr) | Mean Annual Discharge (rain + snow − ET) × $10^3$ ($m^3/s$) | Snowmelt Contribution to Annual Discharge (%) | Evapotranspiration Contribution to Annual Discharge (negative contribution in %) | May–Oct Rainfall Contribution to Annual Discharge (%) | May–Oct Snowmelt Contribution to Annual Discharge (%) |
|---|---|---|---|---|---|---|---|---|
| 1 | Indus (*Pakistan/India/China*) | 205,536 | 0.3 | 4.2 | 65.7 | 2.2 | 26.2 | 61.6 |
| 2 | Jhelum (*Pakistan/India*) | 26,539 | 1.3 | 1.2 | 24.9 | 17.1 | 65.1 | 17.7 |
| 3 | Chenab (*India*) | 21,901 | 1.1 | 1.1 | 43.4 | 7.6 | 43.5 | 38.2 |
| 4 | Ravi (*India*) | 5,562 | 2.4 | 0.4 | 16.1 | 9.0 | 59.1 | 10.2 |
| 5 | Beas (*India*) | 7,644 | 2.0 | 0.5 | 21.3 | 9.0 | 64.9 | 16.5 |
| 6 | Sutlej (*India/China*) | 52,798 | 0.3 | 0.8 | 57.1 | 5.3 | 38.1 | 48.3 |
| 7 | Tons/Yamuna (*India*) | 10,235 | 2.0 | 0.6 | 9.8 | 17.0 | 88.9 | 4.7 |
| 8 | Ganges (*India*) | 21,731 | 1.4 | 1.1 | 22.4 | 12.3 | 75.0 | 18.2 |
| 9 | Mahakali (*India/Nepal*) | 15,216 | 1.8 | 0.8 | 14.4 | 15.2 | 83.6 | 11.3 |
| 10 | Karnali (*Nepal*) | 45,529 | 1.2 | 1.8 | 20.5 | 14.2 | 80.9 | 14.3 |
| 11 | KaliGandaki (*Nepal*) | 11,863 | 2.0 | 0.7 | 10.0 | 11.9 | 87.7 | 7.2 |
| 12 | Seti (*Nepal*) | 2,943 | 3.2 | 0.3 | 2.8 | 11.8 | 92.7 | 1.6 |
| 13 | Marsyandi (*Nepal*) | 4,805 | 2.0 | 0.3 | 15.1 | 7.1 | 74.3 | 11.4 |
| 14 | Trisuli (*Nepal/China*) | 11,688 | 1.6 | 0.6 | 15.0 | 6.5 | 78.8 | 10.3 |
| 15 | Sunkosi (*Nepal/China*) | 18,182 | 1.9 | 1.1 | 8.6 | 7.7 | 79.3 | 6.3 |
| 16 | Arun (*Nepal/China*) | 33,578 | 0.5 | 0.6 | 24.7 | 5.5 | 69.2 | 19.4 |
| 17 | Tamur (*Nepal*) | 6,102 | 1.8 | 0.3 | 7.1 | 10.3 | 90.6 | 4.7 |
| 18 | Tista (*Nepal*) | 8,166 | 1.9 | 0.5 | 8.2 | 9.1 | 86.9 | 5.3 |
| 19 | Amo (*Nepal/Bhutan*) | 3,285 | 2.0 | 0.2 | 10.5 | 8.1 | 80.9 | 5.8 |
| 20 | Wang (*Bhutan*) | 4,597 | 2.3 | 0.3 | 8.4 | 7.3 | 89.1 | 4.1 |
| 21 | PunaTsang (*Bhutan*) | 9,688 | 1.6 | 0.5 | 10.4 | 10.2 | 90.2 | 6.4 |
| 22 | Mangde/Chamkhar (*Bhutan*) | 7,432 | 1.5 | 0.4 | 10.4 | 12.4 | 90.5 | 6.2 |
| 23 | Manas (*Bhutan/China*) | 21,061 | 0.8 | 0.6 | 24.6 | 10.9 | 75.7 | 17.0 |
| 24 | Bhareli (*India*) | 9,526 | 1.6 | 0.5 | 9.1 | 17.9 | 91.9 | 5.5 |
| 25 | Subansiri (*India/China*) | 26,245 | 1.3 | 1.1 | 13.6 | 11.5 | 79.4 | 7.7 |
| 26 | Tsangpo (*India/China*) | 255,929 | 0.5 | 5.1 | 34.3 | 4.1 | 59.2 | 29.1 |
| 27 | Dibang (*India*) | 11,271 | 2.2 | 0.8 | 8.6 | 4.8 | 70.4 | 4.4 |
| | | | Mean Annual 2B31 Rainfall (m/yr) | Mean Annual Discharge (rain + snow − ET) × $10^3$ ($m^3/s$) | Snowmelt Contribution to Annual Discharge (%) | Evapotranspiration Contribution to Annual Discharge (negative contribution in %) | May–Oct Rainfall Contribution to Annual Discharge (%) | May–Oct Snowmelt Contribution to Annual Discharge (%) |
| Average (per catchment) | | | 1.6 | 1.0 | 19.2 | 9.9 | 74.5 | 14.6 |
| Areal average (all 27 catchments combined) | | | | | 30.4 | 8.0 | 63.0 | 25.5 |

[a]See Figure 1a for locations. Catchments 1 to 6 drain into the Arabian Sea, while all other catchments drain into the Bay of Bengal. Generally, catchments in the far western and somewhat in the eastern Himalaya have a higher snowmelt contribution to discharge then central Himalayan catchments. Negative contribution of evapotranspiration (ET) to annual discharge is linked to catchment vegetation amounts and usually <10%, except for a few, smaller, densely vegetated catchments. Note that rainfall during the summer monsoon (May to October) accounts for ~63% of the annual discharge from the entire Himalaya. In contrast, snowmelt mostly during the early summer season accounts for ~25% of the annual discharge from the Himalaya.

gauged catchments in the Himalaya [*Agarwal et al.*, 1983; *Singh and Quick*, 1993; *Singh et al.*, 1997].

[43] Evapotranspiration plays only a minor role in the high-elevation, mountainous catchments and is generally less than 10% of the total hydrological budget, with a few exceptions of small, densely vegetated, and low-elevation catchments (Table 1 and Figure S5). Importantly, evapotranspiration amounts in the Ganges foreland (not included in this analysis but shown in Figure S5) are up to 30% of rainfall amounts [*Mu et al.*, 2007]. Thus, hydrological studies including the Ganges and Indus foreland must include evapotranspiration as a significant factor within the overall hydrological budget.

[44] Generally, our discharge model successfully predicts both the magnitude of the discharge and the timing of discharge peaks (Figures 10 and 15). Overall, we argue that, despite our model's simplicity, we are able to capture the main components of the hydrological budget of the mountainous Himalaya. Only the combination of the calibrated, high-spatial resolution TRMM rainfall, the MODIS-derived snowmelt model, and MODIS-derived evapotranspiration amounts allows accurate prediction of discharge amounts. The steep, 10-fold, north-south rainfall gradient across the Himalaya and the spatially varying snow cover render lower resolution data much less useful.

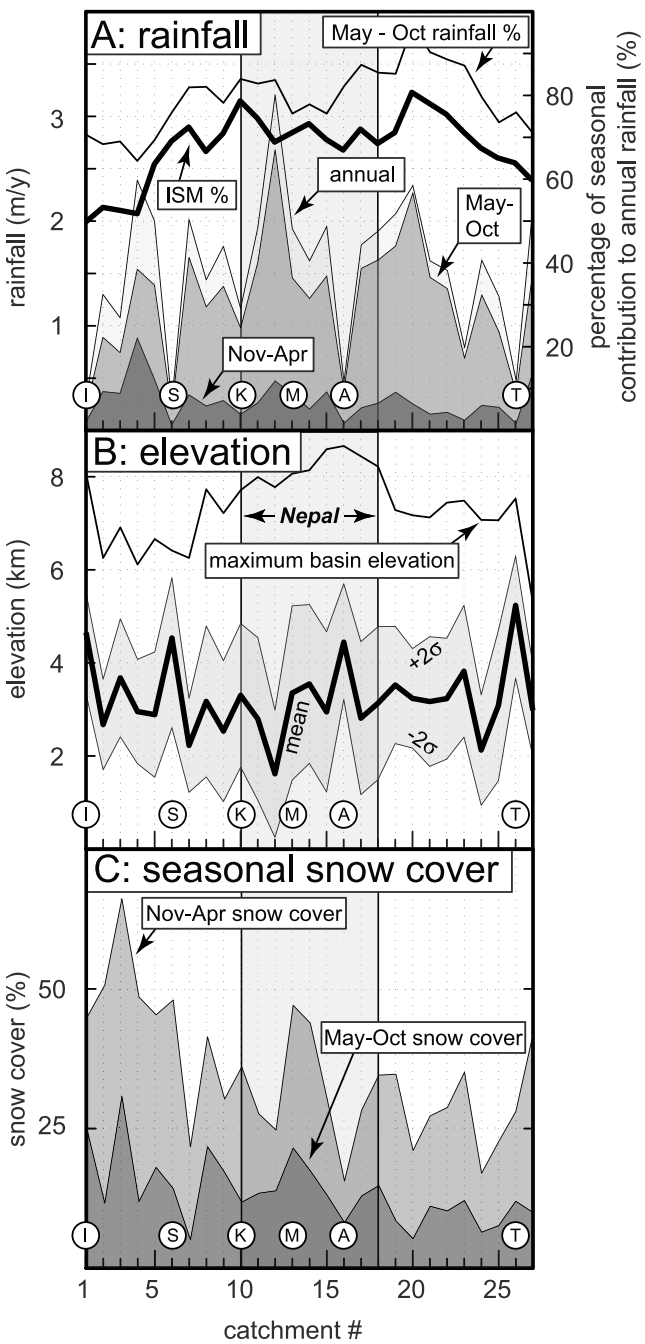


**Figure 12.** (a) Calibrated TRMM-derived summer (May to Oct), winter (Nov to Apr), and annual rainfall. Central and eastern catchments are dominated by the Indian Summer monsoon (ISM, here June to September and the extended summer season from May to October) with no apparent along-strike rainfall gradient. Note that large parts (>50%) of the Indus, Sutlej, Arun, and Tsangpo catchments lie within the dry Tibetan dry zone. (b) Mean elevations (gray shading $\pm 2\sigma$) show little variation along strike (with the exception of the smaller catchments Seti #12 and Bhareli #24), whereas most of the maximum elevations of major peaks occur in the central Himalaya. (c) Average fraction of catchment covered with snow based on 8 years of MODIS snow-cover data. Note the general westward increase in snow cover on both a seasonal and annual basis. In combination with reduced rainfall in the western Himalaya (see Figure 12a), the high snow cover area has a pronounced effect on river discharge (Figure 13).

## 5. Discussion

### 5.1. Limits of Remotely Sensed Boundary Conditions

[45] The Himalaya is part of the largest and the highest mountain chain on Earth. Their terrain is hard to access, and it is almost impossible to build a hydrological data set based on presently available field data. Thus, we have used several calibrated remotely sensed data sets to constrain the controlling factors for the hydrological budget. Despite our usage of high spatial resolution data and incorporation of new remote-sensing data sets, several shortcomings in the remote sensing data warrant attention when interpreting the results:

[46] 1. Our data have been derived on spatial scales of ~5 × 5 km$^2$ (rainfall) and ~1 × 1 km$^2$ (snowmelt model, evapotranspiration, solar radiation). This resolution places a natural limit on the minimum catchment area that can be studied and accurately resolved with these data (approximately 100 km$^2$). An additional limit related to the spatial resolution is the areal extent of the data and their dependence on terrain slope; steep terrain has a larger surface area than flat terrain.

[47] 2. The temporal resolution of the data does not provide continuous observations like those derived from in situ field measurements, but rather yields one to several snapshots per day. Given that convective rainstorms in the Himalaya have a relatively short lifetime of a half hour to several hours, the data need to be averaged over several weeks or at month-long timescales to provide statistically robust rainfall amounts. Thus, we have limited our high-spatial resolution rainfall data to mean monthly rainfall

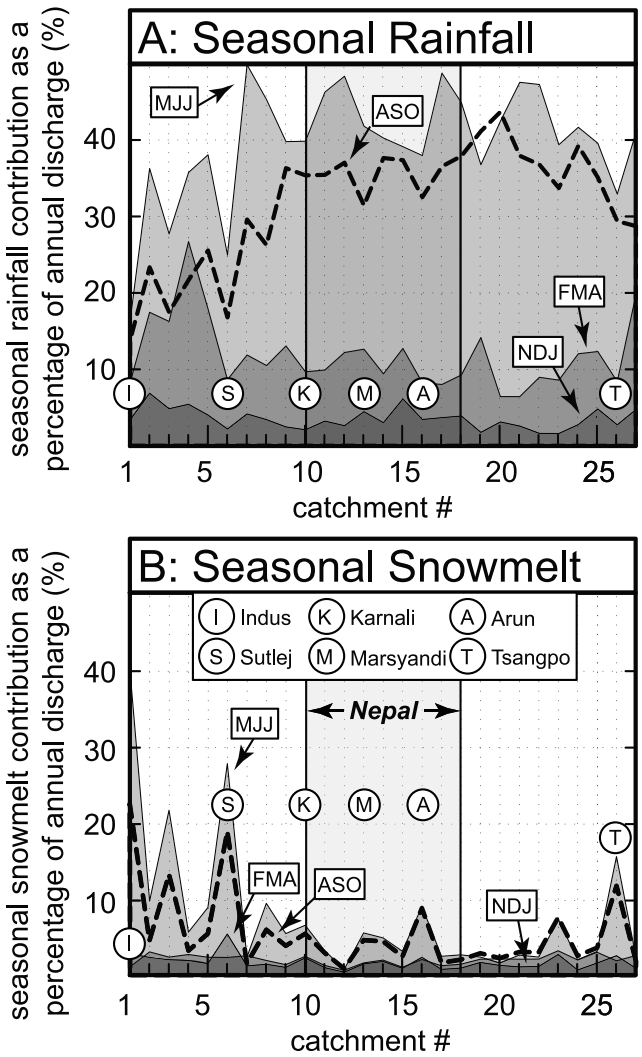


**Figure 13.** (a) Seasonal rainfall and (b) snowmelt contributions to annual discharge. Rainfall during May to July (MJJ) generates 30–40% (in places >45%) of the annual runoff in the central Himalaya. Both early (MJJ) and late summer (August to October, ASO) show a steep gradient with significantly lower contribution in the western catchments. Snowmelt during May to June is an important contribution to the overall annual runoff in western Himalayan and Tsangpo catchments (>10%, and for the Indus, up to 40%). Snowmelt during the winter season contributes only ~5% of the annual runoff. Note that evapotranspiration is not subtracted from rain and snowmelt contribution and therefore rain and snowmelt may add up to >100%.

amounts averaged over the past 10 years. We emphasize that seasonal variation (Figure 13a) may skew this relationship and may explain some of the scatter shown in the calibration processes (Figure 2). In addition, we caution that our temporal precipitation sampling may miss short, but intense storm events and, therefore, our estimates are considered as minimums. Whereas our data represent a significant improvement in the spatial realm over previously used data, they have clear temporal limitations. Previous research has shown that larger catchments (>5 × $10^3$ $km^2$) are not significantly affected by rainfall-sampling errors [*Steiner et al.*, 2003; *Nijssen and Lettenmaier*, 2004]. In addition, recent research indicates that the sampling frequency of the raw, orbital TRMM Precipitation Radar is sufficiently rapid to accurately capture steep rainfall gradients [*Nesbitt and Anders*, 2009].

[48] 3. Similar constraints exist for the observational spatiotemporal scales for the MODIS products. Because dense cloud cover or high water-vapor content in the atmosphere renders some measurements unreliable, we have used data products that average over an 8-day period, which we then smooth to yield monthly averages.

[49] 4. The snowmelt model uses a simple approach to estimate snow-water volumes. Whereas this approach has been shown to be a useful estimator, it certainly neglects several key aspects, such as the distinction between snow and ice (glaciers). However, the contribution of ice melt is in many cases of lesser importance than snowmelt. We have estimated ice-cover extent in the Himalaya with multispectral satellite imagery and identify glacial coverage to be on average 10 to 15% of the snow cover area. In addition, we use the same restricted conversion factor ($a_r$ in equations (1) and (2)) throughout the Himalaya. One could refine this approach by creating spatially varying conversion factors. Such conversion, however, requires rigorous calibration efforts with river-gauge stations and measurements near snow covered or glacierized areas. In the Himalaya, only a few useful river gauges exist because most of the rivers have no measurements at all or have hydropower projects with large dams that alter the water flow, time lag, and evapotranspiration amounts. Whereas our model predicts measured discharge quite well (Figures 3, 10, and 15), our station data provide only limited control on the relative influence of snow- versus rain-fed catchments (Figure 15).

[50] 5. Our hydrological budget approach includes only rainfall, snowmelt, and evapotranspiration as key components. Whereas these processes are likely to dominate, we neglect transient water storage in soils, floodplain, and vegetation, infiltration (losses to the ground), and groundwater fluxes. These and other processes may be important on smaller spatial and shorter temporal scales.

### 5.2. Factors That Control the Rainfall Distribution

[51] Previously, we demonstrated a spatial correlation of elevation or relief with the position of the outer and inner Himalayan rainfall peaks [*Bookhagen and Burbank*, 2006]. Illustrated by three key observations, the analysis presented here suggests that not only rainfall peaks, but also Himalayan rainfall distributions, are closely related to topography and relief. First, integrated rainfall amounts along the mountainous Himalaya do not vary significantly, despite the strong east-to-west rainfall gradient along the foreland (Figure 6b). Thus, the integrated rainfall content (or total water volume) is similar for the two characteristic morphologies of the southern Himalayan front, even though peak rainfall amounts associated with the steep, one-step morphology are higher and on the order of 4–6 m/yr (Figures 7 and 8). Second, high-relief areas in parts of the western and eastern Himalaya (i.e., in the vicinity of the Chenab, Ravi, Amo, Wang, and Puna Tsang catchments) occur along the southern edge of the Himalayan topography (Figure 7). These high-relief areas result in high amounts of rainfall at the mountain

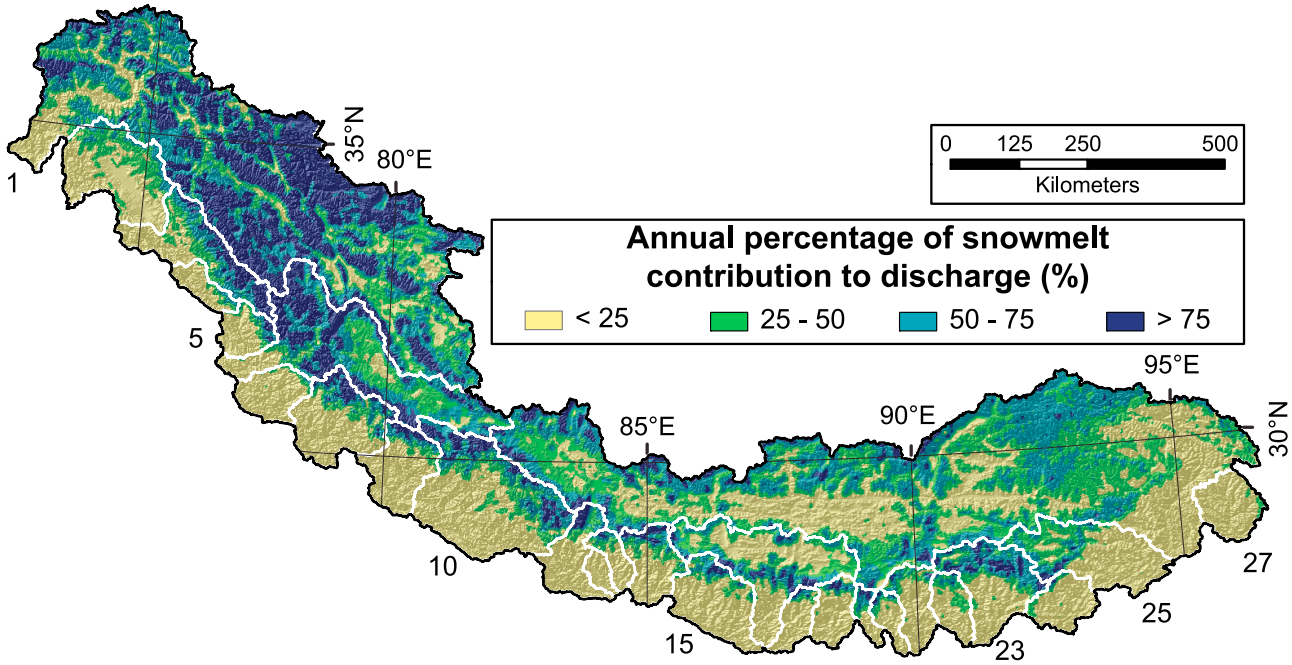


**Figure 14.** Spatial distribution of annual snowmelt contribution to discharge. Note the high percentages derived from snowmelt in the western catchments as well as in the high elevations along the Himalaya. The frontal areas are dominated by rainfall and thus have very low snowmelt contribution.

front. When relief within a 5-km-radius circle exceeds 2 km at or near the mountain front, much of the monsoonal precipitation appears to be efficiently extracted, thereby inhibiting the formation of a second, more northerly rainfall peak. Thus, the high amount of rainfall in the low-elevation plains in the eastern and western Himalaya is related to the "barrier of relief" that prevents rainfall from penetrating farther into the orogen. Third, the high amount of rainfall in the Higher (Greater) Himalaya in the central Himalaya (i.e., the Kali Gandaki #11, Seti #12, and Marsyandi #13 in Figure 12) is related to at least two factors: (1) the topographic relief both at the mountain front and of the Lesser Himalaya overall is lower, allowing more water vapor (and ultimately rainfall) to penetrate into the orogen, and (2) topographic relief of the Greater Himalaya in these regions is unusually high (more than 4 km as opposed to just above 3 km in equivalent regions to the east and west: Figure 7).

[52] We are able to use topographic (elevation and relief) data to assess the effectiveness of Himalaya-rainfall extraction at a topographic barrier. In order to calculate a rainout ratio perpendicular to the mountain front, we assume that the total rainfall amount is the sum of all TRMM-derived rain in the mountains, i.e., above 500 m elevation. The rainout ratio is somewhat similar to the drying ratio described by *Smith and Evans* [2007], which is defined as the fraction of the incoming water vapor flux that is rained out over the mountains. Because we cannot directly measure atmospheric moisture, we refer instead to "rain water," which constitutes the summed TRMM-derived rainfall that occurs downwind of any point in a swath. We calculate a rainout ratio for each rainfall peak within the fifty, 50-km-wide swaths (swath locations are shown in Figure 7a). The rainfall peak defines the center of a 50-km-long area (25 km on each side) under which we integrate rainfall (i.e., rainfall loss from the atmosphere), as well as average topographic elevation and 5-km-radius relief amounts. The rainout ratio for each 50-km-long area is thus the amount of rainfall within the area divided by the total amount of water in the air column (at the upwind edge of that area) that will ultimately be rained out within any swath. This ratio captures the efficiency of rainfall extraction within the rainfall peak and may provide an initial step toward quantifying a topography-rainfall relation. We find a robust relation between the rainout ratio and relief (Figure 16) suggesting that higher relief results in higher rainout ratios: an increase in relief by 1 km results on average in a rainout-ratio increase of ~25%. This rainfall-relief relation appears valid along the southern Himalayan front and explains the variations in peak-rainfall magnitudes along strike (Figures 4a and 7): generally, relief amounts and rainfall at the range front are higher in the eastern and western

**Figure 15.** (a) Sutlej River region (catchment #6 in Figure 1), showing gauging stations 1 to 3. Annual hydrographs for (b) the high-elevation, northeastern section of the catchment (site 1), (c) the moderate-elevation section (site 2), and (d) the low-elevation section (site 3). Dashed lines indicate gauged discharge and light gray coloring outlines predicted discharge from the rainfall (blue circles) and evapotranspiration (green squares) data and snowmelt model (orange crosses). Note that evapotranspiration amounts are a negative term in the hydrologic budget. Generally, the model predicts discharges well. (e) Area versus elevation for the Sutlej River. Note horizontal steps result from tributary junctions. Discharge measurements of gauging stations 1–3 shown on the right axis.

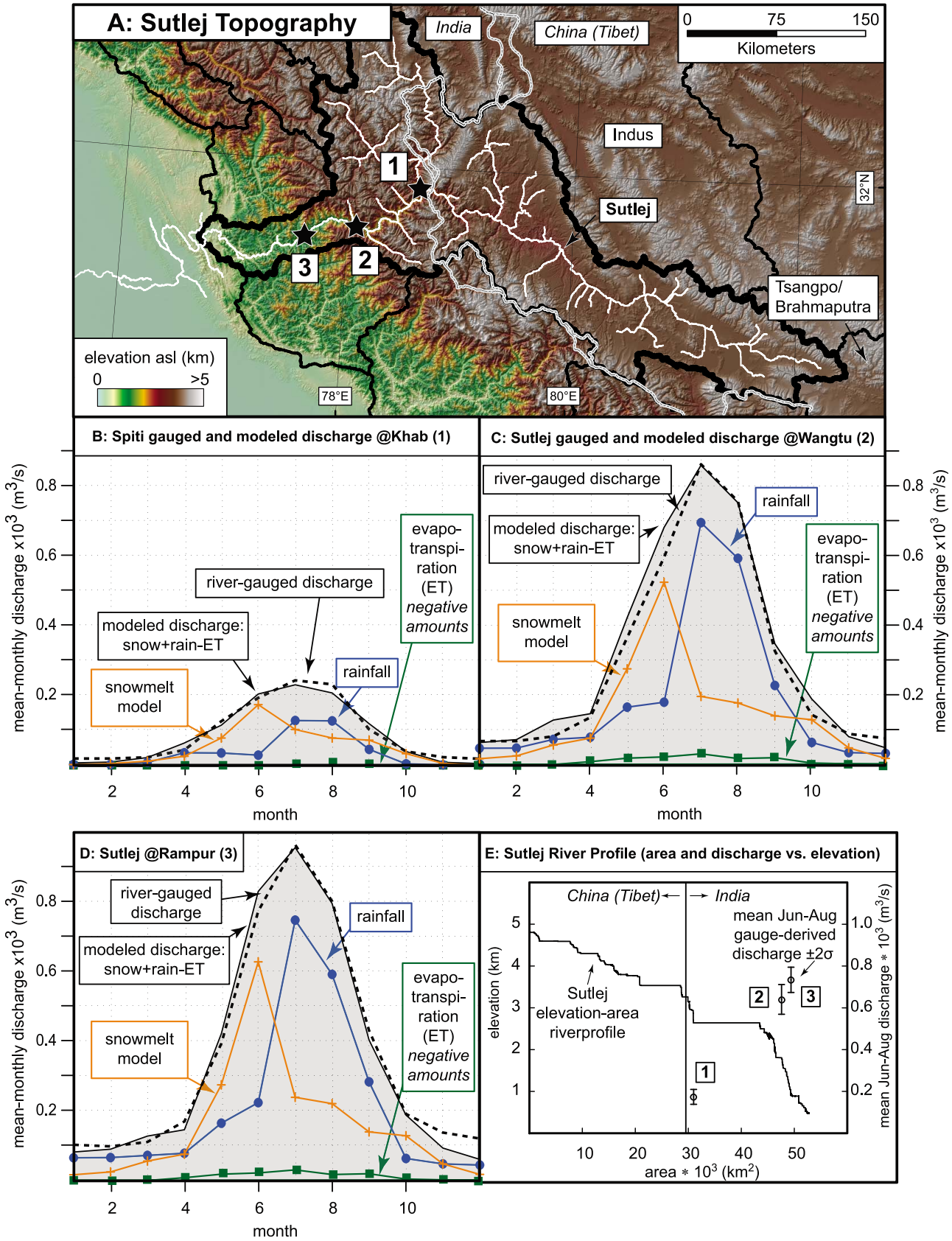
A: Sutlej Topography
India
China (Tibet)
0 75 150
Kilometers
Indus
Sutlej
Tsangpo/
Brahmaputra
32°N
78°E
80°E
1
2
3
elevation asl (km)
0 >5
B: Spiti gauged and modeled discharge @Khab (1)
C: Sutlej gauged and modeled discharge @Wangtu (2)
D: Sutlej @Rampur (3)
E: Sutlej River Profile (area and discharge vs. elevation)
river-gauged discharge
modeled discharge: snow+rain-ET
snowmelt model
rainfall
evapo-transpi-ration (ET) negative amounts
mean-monthly discharge x10^3 (m^3/s)
month
China (Tibet) ← → India
Sutlej elevation-area riverprofile
mean Jun-Aug gauge-derived discharge ±2σ
elevation (km)
area * 10^3 (km^2)
mean Jun-Aug discharge * 10^3 (m^3/s)

**Figure 15**

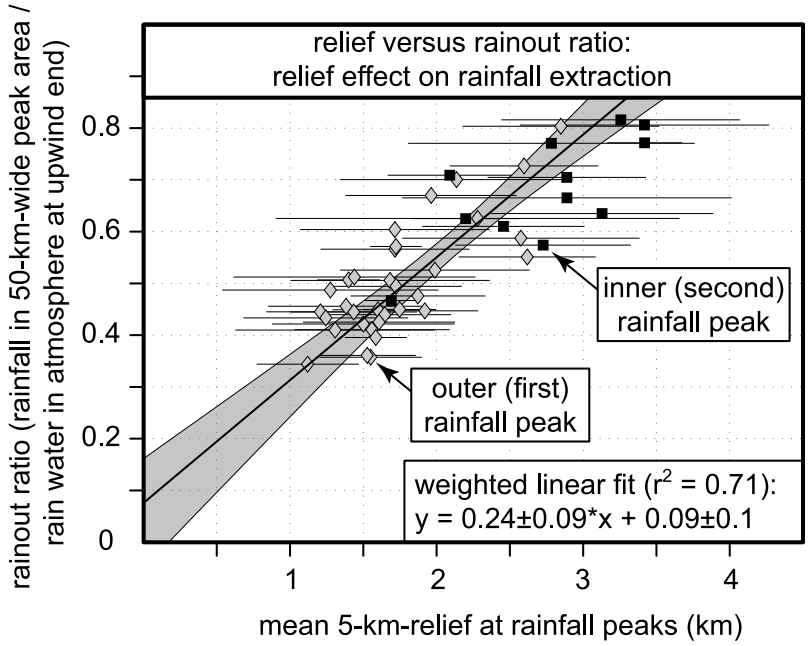


**Figure 16.** Relief versus rainout ratio for 50-km-wide swaths (see Figure 8 for swath-profile location). Rainout ratio (ratio of peak-rainfall amounts to upwind volume of rainwater in the atmosphere at the upwind end) indicates how much rainfall is lost across a 50-km-long zone that is centered on the highest rainfall peak(s) in each swath. Alternatively, the rainout ratio can be viewed as the fraction of incoming rainwater removed in the 50-km-wide peak area. Horizontal lines indicate the 1-sigma standard deviation of relief under the rainfall area. Relief is measured with a 5-km radius for each pixel and averaged across the swath. This correlation suggests that relief is a moderately robust ($r^2 = 0.71$) indicator for orographic-barrier efficiency. Outer (first) rainfall peaks lose more than 40% of their rainfall in areas with 1.5–2 km of relief, whereas an orographic barrier at the Himalayan front with 3-km relief is predicted to cause an ~80% loss of the upwind rainwater (rainout ratio of ~0.8).

Himalaya than in the central part of the range [*Bookhagen and Burbank*, 2006].

[53] We recognize that rain falls over Tibet beyond the end of our swaths. To the extent that Tibetan rainfall derives from storm paths that trend across the Himalaya from the foreland, our calculations underestimate the total amount of rainwater at the upwind end of a swath and, therefore, overestimate the efficiency of rainfall extraction within the

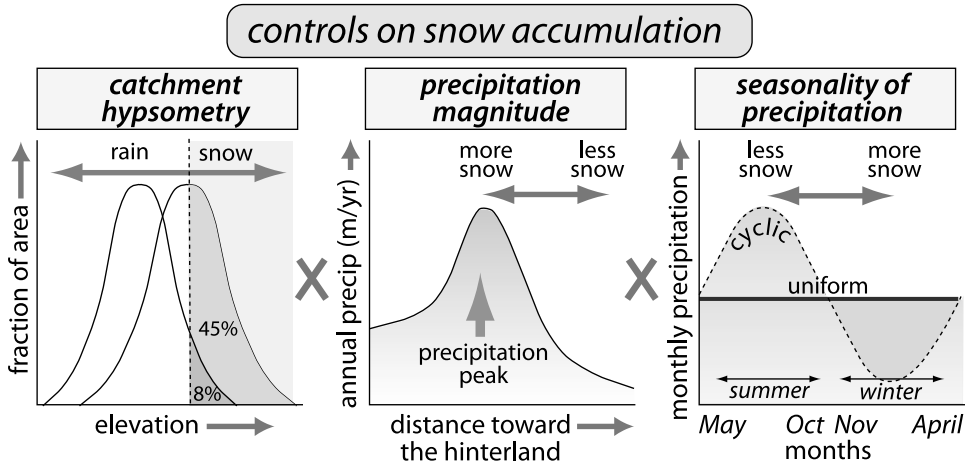


**Figure 17.** Conceptual summary of the three dominant factors exerting control on snow accumulation and hence snowmelt generation in mountainous regions: (1) Catchment hypsometry or elevation distribution within a catchment, (2) spatial distribution of precipitation magnitude, (3) seasonality or temporal distribution of precipitation. Higher topography, greater proximity to the precipitation peak, and a higher fraction of winter precipitation all lead to more snow accumulation.

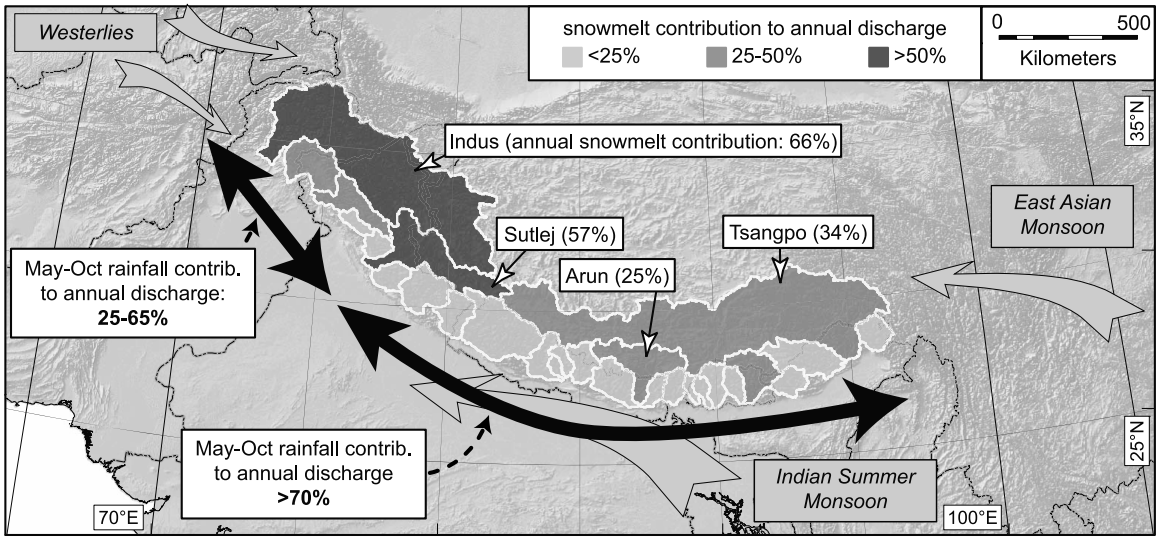


**Figure 18.** Conceptual climatic and hydrologic model for the Himalaya. Light gray shading of Himalayan catchments primarily in the central and eastern Himalaya indicate snowmelt contribution of <25% to annual discharge. Moderate to high snowmelt contribution occur in catchments with significant winter snow cover (e.g., Indus, Sutlej, Arun and Tsangpo). Black arrows indicate catchment and their corresponding summer (May to October) rainfall amounts: western catchments receive <65% of their annual discharge from rainfall (Indus: 40%), whereas catchments to the east of the Sutlej receive >70% of their annual discharge from rainfall. Gray arrows indicate major moisture-source directions.

swath. Given the multiple potential sources for rainfall and the overall small amount of total Himalayan-Tibetan rainfall that is represented by rainfall over Tibet, we argue that our simplified treatment, in which we consider only measured rainfall within a swath, is justified.

### 5.3. Spatial and Temporal Rainfall and Snowmelt Variability: Implications for Erosion

[54] Recent studies suggest that both annual rainfall and its temporal distribution modulate erosion rates [e.g., *Snyder et al.*, 2003]. This dual dependency results because erosion of channels and hillslopes is in many cases a threshold phenomenon: a minimum rainfall intensity must be surpassed before erosion takes place; and high intensity events contribute disproportionately to erosion [e.g., *Gabet et al.*, 2004; *Lague et al.*, 2005; *Snyder et al.*, 2003; *Whipple*, 2004]. We show here that (1) maximum rainfall intensity and lightning frequency generally co-vary spatially and (2) zones of maximum intensity do not necessarily correlate with zones of high annual rainfall. Notably, the largest area of high intensity rainfall occurs in the northwest Himalaya (Figure 8) where the average monsoonal rainfall (Figures 4 and 12) is considerably less than in the central Himalaya. These high-intensity storms in the NW Himalaya have the potential to sustain rapid erosion, despite the overall drier climate.

[55] Interannual variability in precipitation has differing effects depending on a catchment's position along the Himalayan front. For example, we identify the Sutlej valley (catchment 6 in Figures 11, 12, and 13) as a transition zone in the Indian summer monsoon circulation system, where rainfall transported westward from the Bay of Bengal becomes less dominant. *Barros et al.* [2004] made similar observations, but suggested that the transition occurs ~150 km farther east near the Garhwal Himalaya in the vicinity of the Ganges valley. Irrespective of any direct link to rainfall, the large-scale Himalayan morphology changes to the west of the Sutlej Valley, such that high topographic relief is developed at the mountain front (Figure 7). This relief prevents the formation of an interior, second rainfall belt, thereby creating a rainfall pattern similar to that which we observe in the vicinity of Bhutan.

[56] Where peak rainfall amounts occur in conjunction with steep topography, the resulting runoff is likely to impact erosion on the southern flank of the Himalaya and at the southern edge of the Lesser and Greater Himalayan Sequences. Evidence from both weak and strong monsoon years indicates that these rainfall peaks are spatially stationary [*Bookhagen et al.*, 2005a; *Bookhagen and Burbank*, 2006]. During large storms, however, more rainfall penetrates into drier areas, and the magnitude of the average, south-to-north rainfall gradient is decreased [*Craddock et al.*, 2007; *Wulf et al.*, 2010]. Our TRMM-derived rainfall intensity measurements support this finding. Previously, we showed that large, synoptic storms during stronger monsoon years enhance the rainfall in the high-elevation areas [*Bookhagen et al.*, 2005a; *Wulf et al.*, 2010]. Similarly, the intensified monsoon phases during the early Holocene are interpreted to have swept more rainfall and water vapor into the high-elevation regions [*Bookhagen et al.*, 2005a; *Bookhagen et al.*, 2005b; *Gasse et al.*, 1991; *Pratt et al.*, 2002]. To the extent that high topographic relief exists in the Himalayan rain shadow, our relief-rainfall analysis (Figure 16) suggests that this relief will tend to focus precipitation in specific regions [*Brozovic et al.*, 1997]. Thus, during intensified monsoon periods, the resultant enhanced discharge should mobilize more sediment and augment erosion rates within these normally arid regions [*Bookhagen et al.*, 2006; *Wulf et al.*, 2010]. Overall, in times of strength-

ened monsoons, we suggest a change of the 'rainfall-tail length' that will enhance rainfall and probably erosion several fold in the high-elevation, high-relief (and usually dry) areas, but will not change the location of major peaks in rainfall along the southern flank of the Himalaya.

[57] Our snowmelt model indicates that the annual snowmelt contribution to discharge is most pronounced in the high elevations of the western Himalaya, as well as in a dozen-kilometer-wide swath encompassing the high summits of the main Himalayan chain (Figure 14b). The southern parts of the Himalayan catchments receive most of their annual hydrological budget as rainfall during summer months. Large quantities of water are stored in the form of snow in the high elevation and western parts of the Himalaya and their release does not occur until several months later in the pre- and early monsoon season. This rapid release of meltwater from March to June leads to serious flooding problems in the Ganges foreland [e.g., *Sharma et al.*, 1991].

[58] Three dominant factors modulate snow accumulation and areal cover (Figure 17): (1) the elevation distribution within a catchment (hypsometry); (2) the magnitude of precipitation; and (3) the seasonality of precipitation (temporal distribution of precipitation). Higher topography experiences lower temperatures, greater proximity to the peak precipitation leads to greater total precipitation (some of which will fall as snow), and a higher fraction of winter precipitation within the annual cycle all promote more snow accumulation and areal cover. Notably, in comparison to summer storms, dampened convection during winter storms reduces the efficiency of rainfall extraction by topography (rainout ratio: Figure 16) and, consequently, reduces orographic effects, such that winter snowfalls are both more areally extensive and uniform in amount [*Putkonen*, 2004; *Wulf et al.*, 2010]. The distinctive hypsometry of the two large western catchments (Indus, Sutlej) in conjunction with their relatively high winter precipitation supply results in large snow accumulation and expansive snow cover. In contrast, the hypsometrically similar Arun catchment in the central Himalaya is monsoon-dominated, receives lower winter precipitation, and, therefore, displays an areally restricted snow cover.

## 6. Conclusion

[59] We combine several new data sets in an attempt to increase our understanding of the spatiotemporal discharge distribution across the Himalaya. First, we analyzed 10 years of high-resolution rainfall data from the Tropical Rainfall Measurement Mission (TRMM) to create an unprecedented overview of modern, spatiotemporal variations in Himalayan monsoonal precipitation. We improved our processing algorithms of orbital data to re-project all swaths onto an equally spaced grid. After this correction and calibration with more than 1700 rain gauges, a coherent rainfall map emerges for the entire Himalaya. When we separate seasonal rainfall amounts and quantify rainfall gradients, two striking gradients emerge: a sixfold east-to-west rainfall gradient along the Himalayan foreland; and a ten-fold south-to-north gradient across the Himalayan range. From a seasonal perspective, most of the Himalaya and Tibet receive more than 80% of their rainfall during the Indian summer monsoon from May to October, but the eastern and western syntaxes, where the Tsangpo and Indus rivers exit the range, receive significant precipitation during the winter months as well. The seasonal east-to-west rainfall gradient divides near the Sutlej valley in the western Himalaya: all catchments to the east (and thus all catchments draining into the Bay of Bengal) receive ~70% of their annual rainfall during the Indian Summer Monsoon (June to September). All catchments to the west of the Sutlej receive less than 50% of their annual rainfall during the summer months (Figure 18).

[60] Second, we show that rainfall within the Himalaya itself – despite strong rainfall gradients along the foreland – is dominated by topography. Whereas the total amount of rainfall that penetrates into the mountainous Himalaya remains nearly constant along strike, the spatial rainfall distribution within the mountains varies widely. We identify two topographic end-members (steadily rising versus two-stepped topography) that correlate with either a single rainfall peak at the range front or two rainfall peaks: one at the range front and one near the toe of the Greater Himalaya. We conclude that topographic relief reliably predicts the efficiency of rainfall extraction within the Himalaya: higher relief causes a higher rainout rate.

[61] Third, we have used the Lightning Image Sensor (LIS) onboard the TRMM platform to create the first coherent lightning map of the Himalaya and to identify regions in the Himalaya with abnormally high lightning activity. These areas indicate vigorous atmospheric convection and generally correlate with intense storm events. In Pakistan and NW India, both the far western frontal region and the medium-to-high elevation Himalayan regions have some of the highest documented lightning rates on Earth with more than 65 lightning strikes per $km^2$ per year. Rates almost as high are observed just south of the Shillong Plateau, one of the wettest places on Earth. The general spatial pattern of the lightning rates is mimicked by a rainfall intensity map that shows maximum hourly rainfall intensities during the 10-year period. Despite along-strike variations in mean annual rainfall, average rainfall intensities remain rather constant. In the outer rainfall band along the Himalayan front, intensities are on the order of 60–80 mm/hr, regardless of the mean rainfall amounts. Rainfall intensities of the inner rainfall peak in the central Himalaya are generally lower: ~30 to 60 mm/hr. We show that extreme rainfall events (relative to average local rainfall) are more common in drier areas. Thus, during strengthened monsoons, southern Tibet is expected to receive both more common and more intense storms, even though the zones of highest rainfall will remain spatially stationary on the southern Himalayan flank.

[62] Fourth, we create a simple, but robust snow-runoff model based on satellite-derived data. This model relies on MODIS-derived snow cover and temperature data, and it includes a solar radiation component calculated from the digital topography. The snowmelt model is a significant step forward in regional runoff modeling for the Himalaya because it assigns a snow cover, temperature, and solar radiation value to each grid cell and does not require subdividing the catchment into areas with similar climatic properties.

[63] Fifth, we combine the snowmelt model with the TRMM-derived rainfall and MODIS-derived evapotranspiration measurements into annual and seasonal river flow estimates. We show that snowmelt accounts for ~50% in the annual runoff budget in the western Himalaya (Indus, Sutlej) (Figure 18). In contrast, the generally smaller central

and eastern Himalaya catchments receive more than 80% of their annual runoff from rainfall and less than 20% from snowmelt (except the large Tsangpo/Brahmaputra catchment which receives ~34% of its annual discharge from snowmelt). Despite the eastward decrease in the contribution of snowmelt to annual runoff, snowmelt is significant and important for all catchments in the pre- and early monsoon months from March to June. During this time, more than 40% of the discharge is derived from snowmelt and is vital to agriculture, hydropower, and water quality throughout the Himalayan foreland.

[64] **Acknowledgments.** The data used in this study were acquired as part of the Tropical Rainfall Measuring Mission (TRMM) sponsored by the Japan National Space Development Agency (NASDA) and the NASA. This work was supported with grants from NASA (NAG5–13758 and NNX08AG05G) and NSF (EAR 9909647 and EAR 0819874). We thank Editor M. Church, Associate Editor S. Mudd, A. Densmore, N. Finnegan, and four anonymous reviewers for reviews and comments.

## References

Agarwal, K. C., et al. (1983), Snowmelt runoff for subcatchment of Beas basin, paper presented at First National Symposium on Seasonal Snow Cover, Snow and Avalanche Study Estab., Manali, India.

Anders, A. M., et al. (2006), Spatial patterns of precipitation and topography in the Himalaya, *Spec. Pap. Geol. Soc. Am.*, *398*, 39–53.

Anderson, E. A. (1973), National weather service river forecast system: Snow accumulation and ablation mode, *NOAA Tech. Memo.*, *NWS HYDRO–17*.

Arnold, J. G., and N. Fohrer (2005), SWAT2000: Current capabilities and research opportunities in applied watershed modelling, *Hydrol. Processes*, *19*, 563–572, doi:10.1002/hyp.5611.

Barnett, T. P., et al. (2005), Potential impacts of a warming climate on water availability in snow-dominated regions, *Nature*, *438*, 303–309, doi:10.1038/nature04141.

Barros, A. P., et al. (2000), A study of the 1999 monsoon rainfall in a mountainous region in central Nepal using TRMM products and rain gauge observations, *Geophys. Res. Lett.*, *27*(22), 3683–3686, doi:10.1029/2000GL011827.

Barros, A. P., et al. (2004), Probing orographic controls in the Himalayas during the monsoon using satellite imagery, *Nat. Hazards Earth Syst. Sci.*, *4*(1), 29–51, doi:10.5194/nhess-4-29-2004.

Barros, A., et al. (Eds.) (2006), From weather to climate—Seasonal and interannual variability of storms and implications for erosion processes in the Himalaya, *Spec. Pap. Geol. Soc. Am.*, *398*, 17–38.

Beas Bhakra Management Board (B.B.M.B.) (2000), Data for hydrological analyses, report, Chandigarh, India.

Bookhagen, B., and D. W. Burbank (2006), Topography, relief, and TRMM-derived rainfall variations along the Himalaya, *Geophys. Res. Lett.*, *33*, L08405, doi:10.1029/2006GL026037.

Bookhagen, B., and M. R. Strecker (2008), Orographic barriers, high-resolution TRMM rainfall, and relief variations along the eastern Andes, *Geophys. Res. Lett.*, *35*, L06403, doi:10.1029/2007GL032011.

Bookhagen, B., et al. (2005a), Abnormal monsoon years and their control on erosion and sediment flux in the high, and northwest Himalaya, *Earth Planet. Sci. Lett.*, *231*(1–2), 131–146, doi:10.1016/j.epsl.2004.11.014.

Bookhagen, B., et al. (2005b), Late Quaternary intensified monsoon phases control landscape evolution in the northwest Himalaya, *Geology*, *33*(2), 149–152, doi:10.1130/G20982.1.

Bookhagen, B., et al. (2006), Holocene monsoonal dynamics and fluvial terrace formation in the northwest Himalaya, India, *Geology*, *34*(7), 601–604, doi:10.1130/G22698.1.

Boos, W. R., and Z. Kuang (2010), Dominat control of the South Asian monsoon by orographic insulation versus plateau heating, *Nature*, *463*, 218–222, doi:10.1038/nature08707.

Brozovic, N., et al. (1997), Climatic limits on landscape development in the northwestern Himalaya, *Science*, *276*(5312), 571–574, doi:10.1126/science.276.5312.571.

Brubaker, K., et al. (1996), Incorporating radiation inputs into the snowmelt runoff model, *Hydrol. Processes*, *10*, 1329–1343, doi:10.1002/(SICI)1099-1085(199610)10:10<1329::AID-HYP464>3.0.CO;2-W.

Burbank, D. W., A. E. Blythe, J. Putkonen, B. Pratt-Sitaula, E. Gabet, M. Oskin, A. Barros, and T. P. Ojha (2003), Decoupling of erosion and precipitation in the Himalayas, *Nature*, *426*, 652–655, doi:10.1038/nature02187.

Christian, H. J., et al. (1999), The Lightning Imaging Sensor, in *Proceedings of the 11th International Conference on Atmospheric Electricity Held in Guntersville, Alabama, June 7–11, 1999*, *NASA Conf. Publ.*, *209261*, 746–749.

Cleugh, H. A., R. Leuning, Q. Z. Mu, and S. W. Running (2007), Regional evaporation estimates from flux tower and MODIS satellite data, *Remote Sens. Environ.*, *106*(3), 285–304, doi:10.1016/j.rse.2006.07.007.

Craddock, W. H., et al. (2007), Bedrock channel geometry along an orographic rainfall gradient in the upper Marsyandi River valley in central Nepal, *J. Geophys. Res.*, *112*, F03007, doi:10.1029/2006JF000589.

Dimri, A. P. (2006), Surface and upper air fields during extreme winter precipitation over the western Himalayas, *Pure Appl. Geophys.*, *163*(8), 1679–1698, doi:10.1007/s00024-006-0092-4.

Ding, Y. H., and J. C. L. Chan (2005), The East Asian summer monsoon: An overview, *Meteorol. Atmos. Phys.*, *89*(1–4), 117–142.

Easterling, D. R., et al. (2002), Global Daily Climatology Network (GDCN), V1.0, July 2002, http://www.ncdc.noaa.gov/oa/climate/research/gdcn/gdcn.html, Natl. Clim. Data Cent., Ashville, N. C.

Farr, T. G., et al. (2007), The Shuttle Radar Topography Mission, *Rev. Geophys.*, *45*, RG2004, doi:10.1029/2005RG000183.

Fasullo, J., and P. J. Webster (2003), A hydrological definition of Indian monsoon onset and withdrawal, *J. Clim.*, *16*(19), 3200–3211, doi:10.1175/1520-0442(2003)016<3200a:AHDOIM>2.0.CO;2.

Ferguson, R. I. (1999), Snowmelt runoff models, *Prog. Phys. Geogr.*, *23*(2), 205–227.

Finnegan, N. J., G. Roe, D. R. Montgomery, and B. Hallet (2005), A scaling relationship for channel width in bedrock rivers, *Geology*, *33*, 229–232.

Flohn, H. (1957), Large-scale aspects of the "summer monsoon" in south and East Asia, *J. Meteorol. Soc. Jpn*, *75*, 180–186.

Franz, K. J., et al. (2008), Operational snow modeling: Addressing the challenges of an energy balance model for National Weather Service forecasts, *J. Hydrol.*, *360*, 48–66, doi:10.1016/j.jhydrol.2008.07.013.

Gabet, E. J., D. W. Burbank, J. K. Putkonen, B. A. Pratt-Sitaula, and T. Ojha (2004), Rainfall thresholds for landsliding in the Himalayas of Nepal, *Geomorphology*, *63*, 131–143, doi:10.1016/j.geomorph.2004.03.011.

Gadgil, S., et al. (2003), The Indian monsoon and its variability, *Annu. Rev. Earth Planet. Sci.*, *31*, 429–467, doi:10.1146/annurev.earth.31.100901.141251.

Galewsky, J. (2009), Rain shadow development during the growth of mountain ranges: An atmospheric dynamics perspective, *J. Geophys. Res.*, *114*, F01018, doi:10.1029/2008JF001085.

Garbrecht, J., and L. W. Martz (1997), The assignment of drainage direction over flat surfaces in raster digital elevation models, *J. Hydrol.*, *193*, 204–213, doi:10.1016/S0022-1694(96)03138-1.

Gasse, F., et al. (1991), A 13,000-year climate record from western Tibet, *Nature*, *353*, 742–745, doi:10.1038/353742a0.

Güntner, A., et al. (2007), A global analysis of temporal and spatial variations in continental water storage, *Water Resour. Res.*, *43*, W05416, doi:10.1029/2006WR005247.

Hahn, D. G., and S. Manabe (1975), Role of mountains in South Asian monsoon circulation, *J. Atmos. Sci.*, *32*(8), 1515–1541, doi:10.1175/1520-0469(1975)032<1515:TROMIT>2.0.CO;2.

Hall, D. K., and K. A. Casey (2003), The MODIS Snow/Ice Global Mapping Project, http://modis-snow-ice.gsfc.nasa.gov/modis.html, Natl. Snow and Ice Data Cent., Boulder, Colo.

Hall, D. K., et al. (2002), MODIS snow-cover products, *Remote Sens. Environ.* *83*(1-2), 181–194, doi:10.1016/S0034-4257(02)00095-0.

Harper, J. T., and N. F. Humphrey (2003), High altitude Himalayan climate inferred from glacial ice flux, *Geophys. Res. Lett.*, *30*(14), 1764, doi:10.1029/2003GL017329.

Hasnain, S. I. (1999), Runoff characteristics of a glacierized catchment, Garhwal Himalaya, India, *Hydrol. Sci. J.*, *44*(6), 847–854, doi:10.1080/02626669909492284.

Hatwar, H. R., et al. (2005), Prediction of western disturbances and associated weather over western Himalayas, *Curr. Sci.*, *88*(6), 913–920.

Hock, R. (2003), Temperature index melt modelling in mountain areas, *J. Hydrol.*, *282*, 104–115, doi:10.1016/S0022-1694(03)00257-9.

Houze, R. A., et al. (2007), Monsoon convection in the Himalayan region as seen by the TRMM Precipitation Radar, *Q. J. R. Meteorol. Soc.*, *133*, 1389–1411.

Huffman, G. J., et al. (2007), The TRMM multisatellite precipitation analysis (TMPA): Quasi-global, multiyear, combined-sensor precipitation estimates at fine scales, *J. Hydrometeorol.*, *8*(1), 38–55, doi:10.1175/JHM560.1.

Immerzeel, W. W., et al. (2009), Large-scale monitoring of snow cover and runoff simulation in Himalayan river basins using remote sensing, *Remote Sens. Environ.*, *113*(1), 40–49, doi:10.1016/j.rse.2008.08.010.

Ives, J. D., and B. Messerli (1989), *The Himalayan Dilemma: Reconciling Development and Conservation*, John Wiley, London, doi:10.4324/9780203169193.

Kumar, L., et al. (1997), Modelling topographic variation in solar radiation in a GIS environment, *Int. J. Geogr. Inf. Sci.*, *11*(5), 475–497, doi:10.1080/136588197242266.

Kummerow, C., et al. (1998), The Tropical Rainfall Measuring Mission (TRMM) Sensor Package, *J. Atmos. Oceanic Technol.*, *15*, 809–817, doi:10.1175/1520-0426(1998)015<0809:TTRMMT>2.0.CO;2.

Kummerow, C., et al. (2000), The status of the Tropical Rainfall Measuring Mission (TRMM) after two years in orbit, *J. Appl. Meteorol.*, *39*(12), 1965–1982, doi:10.1175/1520-0450(2001)040<1965:TSOTTR>2.0.CO;2.

Kundzewicz, Z. W., et al. (2007), Freshwater resources and their management, in *Climate Change 2007: Impacts, Adaptation and Vulnerability. Contribution of Working Group II to the Fourth Assessment Report of the Intergovernmental Panel on Climate Change*, edited by M. L. Parry et al., pp. 173–210, Cambridge Univ. Press, Cambridge, U. K.

Lague, D., et al. (2005), Discharge, discharge variability, and the bedrock channel profile, *J. Geophys. Res.*, *110*, F04006, doi:10.1029/2004JF000259.

Lang, T. J., and A. P. Barros (2002), An investigation of the onsets of the 1999 and 2000 monsoons in central Nepal, *Mon. Weather Rev.*, *130*(5), 1299–1316, doi:10.1175/1520-0493(2002)130<1299:AIOTOO>2.0.CO;2.

Lang, T. J., and A. P. Barros (2004), Winter storms in the central Himalayas, *J. Meteorol. Soc. Jpn.*, *82*, 829–844, doi:10.2151/jmsj.2004.829.

Lemke, P., et al. (2007), *Observations: Changes in Snow, Ice and Frozen Ground*, Cambridge Univ. Press, Cambridge, U. K.

Linsley, R. K., Jr. (1943), A Simple procedure for the daily forecasting of runoff from snowmelt, *Eos Trans. AGU, Part III*, *24*, 62–67.

Magagi, R., and A. P. Barros (2004), Estimation of latent heating of rainfall during the onset of the Indian monsoon using TRMM PR and radiosonde data, *J. Appl. Meteorol.*, *43*(2), 328–349, doi:10.1175/1520-0450(2004)043<0328:EOLHOR>2.0.CO;2.

Martinec, J., et al. (2007), *Snowmelt Runoff Model (SRM): User's Manual*, 175 pp., N. M. State Univ., Las Cruces.

Monteith, J. L. (1964), Evaporation and environment, in *The State and Movement of Water in Living Organisms*, edited by B. D. Fogg, pp. 205–234, Cambridge Univ. Press, Cambridge, U. K.

Mu, Q., F. A. Heinsch, M. Zhao, and S. W. Running (2007), Development of a global evapotranspiration algorithm based on MODIS and global meteorology data, *Remote Sens. Environ.*, *111*(4), 519–536, doi:10.1016/j.rse.2007.04.015.

Nash, J. E., and J. V. Sutcliffe (1970), River flow forecasting through conceptual models part I–A discussion of principles, *J. Hydrol.*, *10*, 282–290, doi:10.1016/0022-1694(70)90255-6.

Nesbitt, S. W., and A. M. Anders (2009), Very high resolution precipitation climatologies from the Tropical Rainfall Measuring Mission precipitation radar, *Geophys. Res. Lett.*, *36*, L15815, doi:10.1029/2009GL038026.

Nijssen, B., and D. P. Lettenmaier (2004), Effect of precipitation sampling error on simulated hydrological fluxes and states: Anticipating the global precipitation measurement satellites, *J. Geophys. Res.*, *109*, D02103, doi:10.1029/2003JD003497.

Parthasarathy, B., et al. (1992), Indian-Summer Monsoon Rainfall Indexes - 1871–1990, *Meteorol. Mag.*, *121*(1441), 174–186.

Petersen, W. A., and S. A. Rutledge (2001), Regional variability in tropical convection: Observations from TRMM, *J. Clim.*, *14*(17), 3566–3586, doi:10.1175/1520-0442(2001)014<3566:RVITCO>2.0.CO;2.

Pratt, B., et al. (2002), Impulsive alluviation during early Holocene strengthened monsoons, central Nepal Himalaya, *Geology*, *30*(10), 911–914, doi:10.1130/0091-7613(2002)030<0911:IADEHS>2.0.CO;2.

Putkonen, J. (2004), Continuous snow and rain data at 500 to 4400 m altitude near Annapurna, Nepal, 1999–2001, *Arct. Antarct. Alp. Res.*, *36*, 244–248, doi:10.1657/1523-0430(2004)036[0244:CSARDA]2.0.CO;2.

Rango, A., and J. Martinec (1995), Revisisting the degree-day method for snowmelt computations, *Water Resour. Bull.*, *31*(4), 657–669.

Rao, S. V. N., et al. (1996), A simple monthly runoff model for snow dominated catchments in western Himalayas, *Nord. Hydrol.*, *27*(4), 255–274.

Riehl, H. (1959), On production of kinetic energy from condensation heating, in *The Atmosphere and the Sea in Motion: Scientific Contributions to the Rossby Memorial Volume*, edited by B. Bolin, pp. 381–399, Rockefeller Inst. Press, New York.

Sharma, P. D., A. K. Goel, and R. S. Minhas (1991), Water and sediment yields into the Sutlej River from the high Himalaya, *Mt. Res. Dev.*, *11*(2), 87–100, doi:10.2307/3673569.

Singh, P., and N. Kumar (1997), Impact assessment of climate change on the hydrological response of a snow and glacier melt runoff dominated Himalayan river, *J. Hydrol.*, *193*, 316–350, doi:10.1016/S0022-1694(96)03142-3.

Singh, P., and M. C. Quick (1993), Streamflow simulation of Satluj River in the western Himalaya, *Snow Glacier Hydrol.*, *218*, 261–271.

Singh, P., S. K. Jain, and N. Kumar (1997), Estimation of snow and glacier-melt contribution to the Chenab River, western Himalaya, *Mt. Res. Dev.*, *17*(1), 49–56, doi:10.2307/3673913.

Smith, R. B., and J. P. Evans (2007), Orographic precipitation and water vapor fractionation over the southern Andes, *J. Hydrometeorol.*, *8*(1), 3–19, doi:10.1175/JHM555.1.

Snyder, N. P., et al. (2003), Importance of a stochastic distribution of floods and erosion thresholds in the bedrock river incision problem, *J. Geophys. Res.*, *108*(B2), 2117, doi:10.1029/2001JB001655.

Steiner, M., et al. (2003), Comparison of two methods for estimating the sampling-related uncertainty of satellite rainfall averages based on a large radar dataset, *J. Clim.*, *16*(22), 3759–3778, doi:10.1175/1520-0442(2003)016<3759:COTMFE>2.0.CO;2.

Sun, Z. G., Q. X. Wang, Z. Ouyang, M. Watanabe, B. Matsushita, and T. Fukushima (2007), Evaluation of MOD16 algorithm using MODIS and ground observational data in winter wheat field in North China Plain, *Hydrol. Processes*, *21*, 1196–1206, doi:10.1002/hyp.6679.

Tarboton, D. G., R. L. Bras, and I. Rodriguez-Iturbe (1991), On the extraction of channel networks from digital elevation data, *Hydrol. Processes*, *5*, 81–100, doi:10.1002/hyp.3360050107.

Viviroli, D., et al. (2007), Mountains of the world, water towers for humanity: Typology, mapping, and global significance, *Water Resour. Res.*, *43*(7), W07447, doi:10.1029/2006WR005653.

Wan, Z., and J. Dozier (1996), A generalized split-window algorithm for retrieving land-surface temperature from space, *IEEE Trans. Geosci. Remote Sens.*, *34*(4), 892–905, doi:10.1109/36.508406.

Wan, Z. M., et al. (2002), Validation of the land-surface temperature products retrieved from Terra Moderate Resolution Imaging Spectroradiometer data, *Remote Sens. Environ.*, *83*(1–2), 163–180, doi:10.1016/S0034-4257(02)00093-7.

Wan, Z., et al. (2004), Quality assessment and validation of the MODIS global land surface temperature, *Int. J. Remote Sens.*, *25*(1), 261–274, doi:10.1080/0143116031000116417.

Wang, B. (2006), *The Asian Monsoon*, 787 pp., Springer, Berlin.

Webster, P. J. (1983), Mechanisms of monsoon low-frequency variability: Surface hydrological effects, *J. Atmos. Sci.*, *40*(9), 2110–2124, doi:10.1175/1520-0469(1983)040<2110:MOMLFV>2.0.CO;2.

Webster, P. J. (1987), *The Elementary Monsoon*, 32 pp., John Wiley, New York.

Webster, P. J., et al. (1998), Monsoons: Processes, predictability, and the prospects for prediction, *J. Geophys. Res.*, *103*(C7), 14,451–14,510, doi:10.1029/97JC02719.

Whipple, K. X. (2004), Bedrock rivers and the geomorphology of active orogens, *Annu. Rev. Earth Planet. Sci.*, *32*, 151–185, doi:10.1146/annurev.earth.32.101802.120356.

Wulf, H., B. Bookhagen, and D. Scherler (2010), Seasonal precipitation gradients and their impact on erosion in the Northwest Himalaya, *Geomorphology*, *118*, 13–21, doi:10.1016/j.geomorph.2009.12.003.

B. Bookhagen, Geography Department, University of California, Santa Barbara, CA 93106, USA.

D. W. Burbank, Institute for Crustal Studies, University of California, Santa Barbara, CA 93106, USA.